Research Paper

GEOSPHERE

GEOSPHERE; v. 12, no. 5

doi:10.1130/GES01293.1

13 figures; 2 tables; 5 supplemental files

CORRESPONDENCE: kyle.larson@ubc.ca

CITATION: Larson, K.P., Kellett, D.A., Cottle, J.M., King, J., Lederer, G., and Rai, S.M., 2016, Anatexis, cooling, and kinematics during orogenesis: Miocene development of the Himalayan metamorphic core, east-central Nepal: Geosphere, v. 12, no. 5, p. 1575–1593, doi:10.1130/GES01293.1.

Received 12 November 2015
Revision received 9 June 2016
Accepted 5 August 2016
Published online 23 August 2016



# Anatexis, cooling, and kinematics during orogenesis: Miocene development of the Himalayan metamorphic core, east-central Nepal

**Kyle P. Larson[1], Dawn A. Kellett[2], John M. Cottle[3], Jess King[4], Graham Lederer[3,*], and Santa Man Rai[5]**

[1]Earth and Environmental Sciences, University of British Columbia Okanagan, FIP353-3247 University Way, Kelowna, British Columbia V1V 1V7, Canada
[2]Geological Survey of Canada, 601 Booth Street, Ottawa, Ontario K1A 0E8, Canada
[3]Department of Earth Science, 1006 Webb Hall, University of California–Santa Barbara, Santa Barbara, California 93106-9630, USA
[4]Department of Earth Sciences, University of Hong Kong, Pokfulam Road, Hong Kong
[5]Department of Geology, Tri-Chandra Campus, Tribhuvan University, Kathmandu, Nepal

## ABSTRACT

**The exposed mid-crustal rocks of the Himalayan orogen provide a natural laboratory for constructing the kinematic evolution of the mid-crust during a large-scale continental collision. Kinematic models provide testable, geometrically valid, internally consistent, integrated solutions for diverse geological data from deformed regions. We investigated the Tama Kosi region of east-central Nepal with structural, geochemical, and geochronological methods to refine a detailed kinematic model for the Miocene Epoch, during which the mid-crust was pervasively deformed, translated southward, and progressively stacked via basal accretion. Geochemical and U-Pb zircon data demonstrate that two similar orthogneiss bodies were derived from different protoliths, one formed through vapor-absent melting at 1940 ± 16 Ma and the other via vapor-present melting at 1863 ± 14 Ma, respectively, indicating that they do not reflect structural repetition. In situ Th-Pb monazite petrochronology from the Mahabharat Range links the orogenic foreland to the exposed mid-crust of the High Himalaya via a coeval, protracted metamorphic growth–crystallization and/or recrystallization record spanning late Eocene or early Oligocene to early Miocene. Differential cooling of white mica, evidenced by $^{40}Ar/^{39}Ar$ cooling ages across the studied area, may outline a previously unrecognized out-of-sequence thrust, the occurrence of which is coincident with the location of a sharp break previously recognized from quartz crystallographic fabric deformation temperatures. Together with previous work, these data form the basis for a new, internally consistent kinematic model for rocks of the Tama Kosi region during the Miocene Epoch that tracks the transition from distributed ductile deformation in the mid-crust to deformation along discrete surfaces during their exhumation.**

*Present address: U.S. Geological Survey, National Minerals Information Center, 12201 Sunrise Valley Drive, MS 988, Reston, Virginia 20192, USA

## INTRODUCTION

The Himalaya forms an arcuate mountain belt that extends for >2000 km from Pakistan in the west to Arunachal Pradesh (India) in the east (Yin and Harrison, 2000). The orogen can be divided into major lithotectonic units separated by large-scale north-dipping structures (Hodges, 2000). From north to south, these include the low metamorphic grade to unmetamorphosed Tethyan sedimentary sequence, which at its base is separated from the high-metamorphic grade Greater Himalayan sequence by the top-to-the-north sense South Tibetan detachment system (Kellett and Grujic, 2012). The Greater Himalaya sequence, in turn, is overthrust on the variably metamorphosed Lesser Himalayan sequence along the southward-propagating Main Central thrust (Gansser, 1964). Metamorphosed rocks from the Lesser Himalayan sequence and the Greater Himalayan sequence together compose the metamorphosed former mid-crustal core of the orogen, the Himalayan metamorphic core (HMC). The base of the Lesser Himalayan sequence is marked by the Main Boundary thrust, which places rocks of the Lesser Himalayan sequence on orogenic molasse sediments of the Siwaliks (Thakur et al., 2010).

Diverse analytical and methodological advances in recent years have provided increasingly complex geological data sets that have led to revised and new interpretations about the dynamic evolution of rocks within collisional orogens. This is particularly true for the Himalayan orogenic system, for which tectonic models have evolved at a rapid pace over the past ~15 yrs. One of the aspects of Himalayan geology that has garnered the most attention over the recent past is the partially synchronous movement across the South Tibetan detachment system and the Main Central thrust (Godin et al., 2006). Thermomechanical simulations of a Himalaya-style collision constructed by Beaumont et al. (2001, 2004) and Jamieson et al. (2004) provide a predictive geodynamic explanation for the development of the opposing-sense structures and the pressure-temperature-time (*P-T-t*) deformation history of the HMC via large-scale lateral ductile flow of the mid-crust during the Miocene. The accumulation

of detailed *P-T-t* data in service of testing the thermomechanical simulations against the geological record, and against alternative published models of the Himalaya contributed to the discovery of numerous tectonometamorphic discontinuities within the HMC, i.e., thrust faults marked by abrupt changes in *P-T-t* pattern but with little to no field expression (e.g., Groppo et al., 2009; Carosi et al., 2010; Larson et al., 2010, 2011). The growing recognition of these structures has fueled further focused *P-T-t* studies leading to the identification of several similar structures along the length of the orogen (e.g., Yakymchuk and Godin, 2012; Larson et al., 2013, 2015; Montomoli et al., 2013, 2015; Rubatto et al., 2013; Larson and Cottle, 2014; Warren et al., 2014; Cottle et al., 2015).

The density of tectonometamorphic discontinuities indicates a high degree of kinematic complexity within the HMC that has been investigated through the development of new kinematic models (e.g., Montomoli et al., 2013, 2015; Cottle et al., 2015; Larson et al., 2015; He et al., 2015; Carosi et al., 2010). One common feature of these models is the juxtaposition, or stacking, of rock packages that is generally interpreted to have promoted deformation and metamorphism in the associated footwalls. An example of this type of relationship was documented in the Tama Kosi region of east-central Nepal (Fig. 1), where a detailed *P-T-t* pseudosection-based study of rocks on either side of an inferred tectonometamorphic discontinuity outlined syntectonic footwall metamorphism at 610–640 °C and 640–700 MPa at ca. 10–8 Ma (Larson et al., 2013). These data were interpreted to reflect burial during overthrusting of a hanging wall that reached peak *P* (0.7–1.1 GPa) metamorphism in the early Miocene followed by peak *T* (~750 °C) along a clockwise retrograde path into the middle Miocene (ca. 19–14 Ma) (Larson et al., 2013). Subsequent quartz crystallographic fabric (*c*-axis) analyses across the same study area demonstrated dominant top-to-the-south shear sense and a sharp break in deformation temperatures across the approximate position of the discontinuity, from 640 ± 50 °C in the footwall to 515 ± 50 °C in the hanging wall (Larson and Cottle, 2014).

## This Study

While available *P-T-t* and quartz *c*-axis fabric data from the Tama Kosi region show distinct breaks at approximately the same structural position, consistent with the occurrence of a tectonometamorphic discontinuity, it remains unclear how the deformation temperature data relate to the overthrusting model required by the *P-T-t* and shear sense data. In Larson and Cottle (2014) it was demonstrated that deformation temperatures increase almost linearly from 500 ± 50 °C at the lowest structural levels sampled to 640 ± 50 °C ~2 km structurally higher. Farther up structural section in the hanging wall of the tectonometamorphic discontinuity, deformation temperatures decrease sharply to 515 ± 50 °C and increase linearly over a distance of ~2 km to 620 ± 50 °C (Larson and Cottle, 2014). The existence of relatively low deformation temperatures in the immediate hanging wall of the inferred discontinuity implies that either the structure continued to operate significantly after metamorphism of the footwall or that the quartz *c*-axis data actually record a distinct later lower temperature structure. If the latter hypothesis is correct, it opens the possibil-

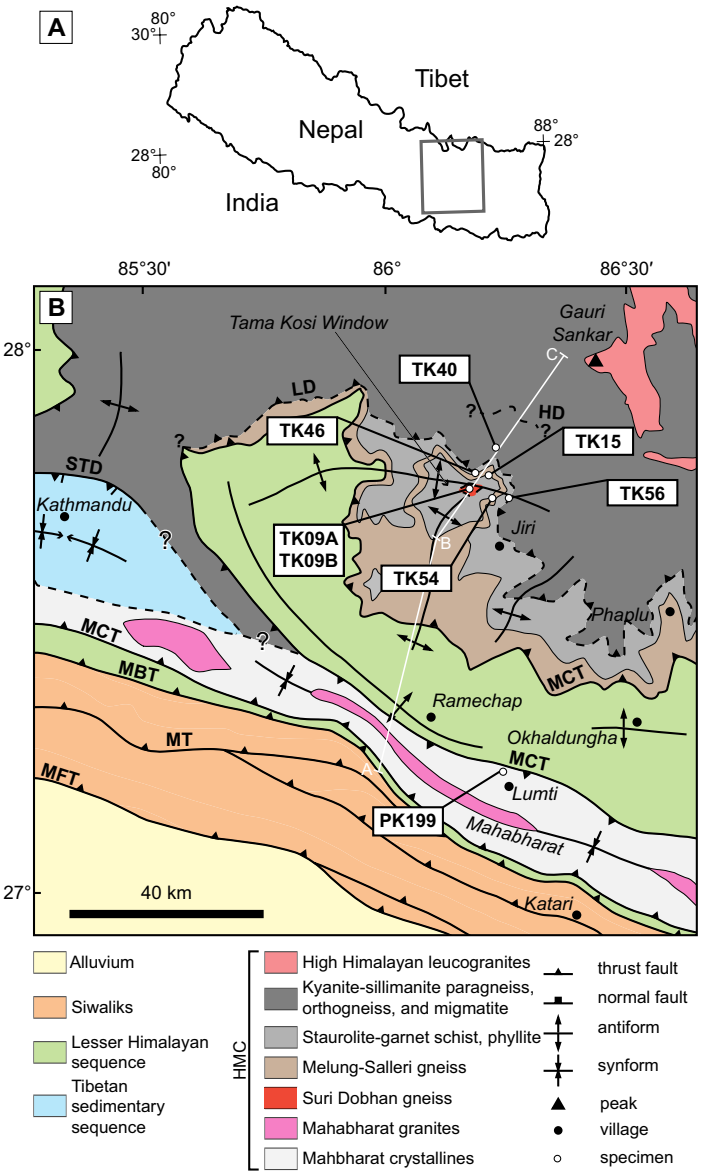


**Figure 1. (A) Location map of the study area. (B) Regional geologic map of east-central Nepal (after Schelling, 1992; Johnson et al., 2001; Larson, 2012; He et al., 2015). Solid white line indicates line of section depicted in Figure 2. Abbreviations: MBT—Main Boundary thrust; MCT—Main Central thrust; MFT—Main Frontal thrust; MT—Marin thrust; STD—South Tibetan detachment; LD—lower discontinuity; HD—higher discontinuity; HMC—Himalayan metamorphic core.**

ity for further, unrecognized structures. For example, based on similar field and mineralogical characteristics, it was postulated that the Suri Dobhan and Melung-Salleri orthogneisses (Fig. 1) could represent a structural duplication of the same unit (Larson, 2012). If there is structural duplication this would necessitate the existence of an additional thrust-sense structure below the documented discontinuity.

We endeavor to construct a geologically accurate kinematic model of the HMC for the Tama Kosi region that captures the known kinematic complexity of the area by investigating outstanding issues: (1) the possible structural repetition of similar orthogneiss units, (2) the possible existence of unrecognized, lower temperature structures in the region, and (3) the inferred genetic relationship between HMC rocks in the Mahabharat foreland region to the south and those in the High Himalaya (Fig. 1; Larson and Cottle, 2014). While the latter interpretation is consistent with some previous interpretations of the rocks of the Mahabharat Range and its equivalents across the Kathmandu nappe to the west (Johnson et al., 2001; Johnson, 2005), others have interpreted that the Mahabharat rocks form a separate, structurally lower thrust sheet (DeCelles et al., 2001) or the hanging wall of a back thrust above the main exhumed mid-crustal core (Webb et al., 2011; He et al., 2015). In order to address these issues we acquired $^{40}Ar/^{39}Ar$ thermochronological data for white mica from specimens in the footwall and hanging wall of the mapped discontinuity to provide constraints on its movement history and look for indications of possible late, low-temperature structures; major and trace geochemical and U/Pb zircon analyses of apparently similar orthogneiss units to assess potential structural repetition; and monazite petrochronological data from a metamorphic rock from the Mahabharat Range.

Our goal in testing and refining a recent kinematic model of the Tama Kosi region is to provide an internally consistent solution to the full kinematic complexity of this portion of the HMC. Until recently, proposed kinematic models of the HMC have been largely, and necessarily, simplistic, typically considering only motion on primary structures such as the Main Central thrust and the South Tibetan detachment system (e.g., Robinson et al., 2006, 2003; DeCelles et al., 2001). Unconstrained variables such as timing of discontinuity formation, structural relationships between lithologically similar units, and correlations between foreland and hinterland kinematics remain ongoing challenges throughout the Himalaya. Reducing these variables requires an incremental and integrated mapping, petrological, geochemical, geochronological, and thermochronological approach. Herein we refine the kinematic model of the Tama Kosi region as a case study for the development of tectonometamorphic discontinuities during shortening of the mid-crust in an orogen, and in this case during the dynamic Miocene Epoch of the Himalayan system (e.g., Cottle et al., 2015; Yin, 2006).

## GEOLOGIC BACKGROUND

The study area was mapped at a reconnaissance scale in the 1960s (Ishida, 1969) and revisited again in the early 1990s (Schelling, 1992). More recent focused mapping (Larson, 2012), augmented by *P-T-t* and quartz *c*-axis fabric analyses (Larson et al., 2013; Larson and Cottle, 2014), built on that existing foundation.

The Tama Kosi region (Fig. 1) is underlain by the pervasively ductilely deformed HMC, which here includes rocks ranging from biotite- and garnet-grade at lowest structural levels in the south to sillimanite-grade migmatite at high structural levels to the north (Schelling, 1992; Ishida, 1969; Larson, 2012). The lowermost tectonometamorphic discontinuity is a thrust structure (identified as LD in Fig. 1) that separates staurolite-grade rocks metamorphosed and deformed at 10–8 Ma from kyanite-grade rocks metamorphosed between ca. 22 and 14 Ma and deformed at a later time (Larson et al., 2013). The structurally higher discontinuity (HD in Fig. 1; also interpreted as a thrust structure) juxtaposes sillimanite-grade rocks with similar early Miocene metamorphic histories on either side; displacement along the structure occurred after peak metamorphism (Larson and Cottle, 2014). These existing geologic data are compatible within a general kinematic framework that includes post-peak metamorphism thrusting at high structural levels and later underplating at lower structural levels (Larson and Cottle, 2014).

## SURI DOBHAN AND MELUNG-SALLERI ORTHOGNEISS UNITS

### Whole-Rock Elemental Geochemistry

The occurrence of two similar orthogneiss units (Suri Dobhan and Melung-Salleri) within the study area (Figs. 1 and 2) may indicate structural duplication (Larson, 2012). To investigate this possibility, one Suri Dobhan and two Melung-Salleri specimens were subjected to whole-rock (X-ray fluorescence; 40 mm loose powder on a Bruker S8 Tiger) and trace element (lithium metaborate fusion and inductively coupled plasma–optical emission spectrometry) analyses at the Saskatchewan Research Council. While we recognize that three specimens do not constitute an exhaustive geochemical study, it does permit us to make some broad interpretations about the respective protoliths.

The Suri Dobhan augen gneiss (Schelling, 1992; Larson, 2012) is the structurally lowest rock unit of the HMC exposed in the mapped area (Figs. 1 and 2). It is strongly deformed and composes the core of the Tama Kosi window (Ishida, 1969), where it is at least 300 m thick (Larson, 2012). The gneiss consists of light to dark gray, fine- to medium-grained quartz (45%), coarse-grained alkali feldspar (25%), plagioclase (16%), muscovite (8%), biotite (6%), and chlorite (1%), and accessory apatite and epidote (estimated from point counting in thin section; Supplemental Fig. 1 in the Supplemental File[1]).

The Melung-Salleri orthogneiss is also strongly deformed and locally augeniferous (alkali feldspar). This gneiss is medium to coarse grained and typically pale to light gray in outcrop. It comprises quartz (42%), alkali feldspar (36%), plagioclase (5%), muscovite (15%), and biotite (2%) with accessory minerals zircon, epidote, and tourmaline (Supplemental Fig. 1; footnote 1). This gneiss commonly exhibits a well-developed S-C fabric with a top-to-the-south sense of shear. The unit is ~1 km thick where mapped within the Tama Kosi

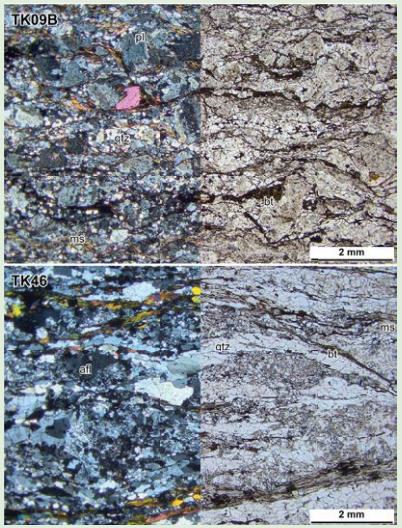


[1]Supplemental File. Details of the U-Th-Pb and $^{40}Ar/^{39}Ar$ methodologies, X-ray maps of all monazite grains analyzed in this study, and $^{40}Ar/^{39}Ar$ step-heating inverse isochron plots. Please visit http://dx.doi.org/10.1130/GES01293.S1 or the full-text article on www.gsapubs.org to view the Supplemental File.

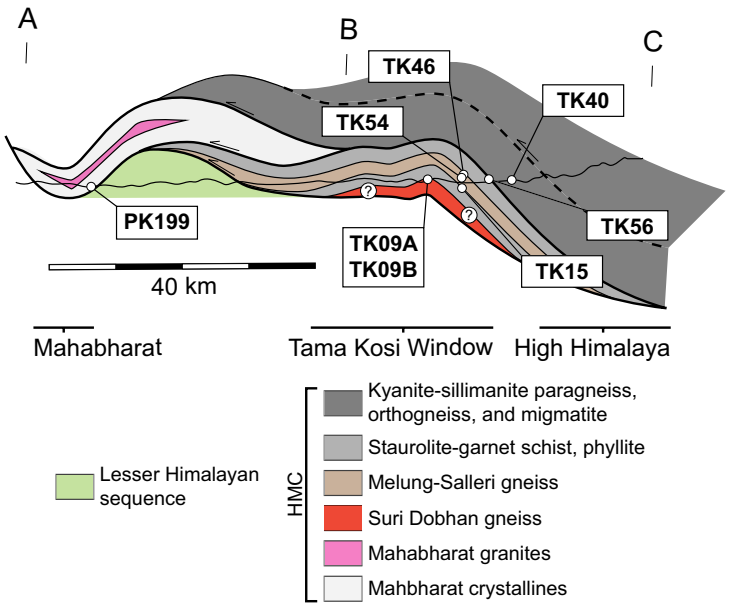


**Figure 2. Generalized approximately southwest–northeast vertical section through the mapped area. The line of section is indicated by a solid white line in Figure 1; legend as in Figure 1. Specimen location is shown as projected into the line of section. Topography is indicated by thin black line; no vertical exaggeration. HMC—Himalayan metamorphic core.**

valley and folds over the top of the Tama Kosi window (Fig. 2; Larson, 2012). Its appearance, gross mineralogy, and texture are comparable to the Suri Dobhan augen gneiss (Schelling, 1992), the Phaplu augen gneiss of the Dudh Kosi (e.g., Jessup et al., 2006), and the Ulleri augen gneiss of west Nepal (Schelling, 1992).

### *Major Element Results and Interpretation*

Representative chemical compositions of the two orthogneiss bodies are presented in Table 1. The $SiO_2$ content ranges from 65.2 to 68.3 wt%, whereas the total alkali content ranges from 7.98 (Suri Dobhan augen gneiss, TK09B) to 8.04 wt% (Melung-Salleri augen gneiss, TK46, TK54), placing them in the trachyte-trachydacite field of the International Union of Geological Sciences classification diagram (Fig. 3A) and granite field on a QAP (quartz, alkali feldspar, plagioclase feldspar) diagram (Fig. 3B). The orthogneiss specimens plot close to the boundary on the Fe* diagram ($Fe^{tot}O/[Fe^{tot}O + MgO]$ vs. $SiO_2$) of Frost et al. (2001), with the Melung-Salleri augen gneiss displaying a stronger ferroan association, while the Suri Dobhan augen gneiss is within the magnesian field (Fig. 3C). Both units are within the alkali field of the modified alkali index (MALI; Frost et al., 2001). In general, for evolving comagmatic suites, the MALI increases with increasing weight percent $SiO_2$ as magma fractionates. This results in genetically related suites plotting an evolution trend along the fields: calcic, calc-alkalic, alkali-calcic, or alkalic, where the delineations are based on common plutonic compositions (Frost et al., 2001). Plotting with almost no MALI variation with increasing $SiO_2$ rather suggests that even though TK46 and TK54 are both ferroan, they do not appear to be cogenetic. These observed differences may alternatively reflect the variable contribution of a crustal component.

TABLE 1. CHEMICAL COMPOSITION OF ORTHOGNEISSES, TAMA KOSI VALLEY, NEPAL

| Specimen | TK09B | TK46 | TK54 |
|---|---|---|---|
| | Major elements (wt% oxide) | | |
| $Na_2O$ | 2.91 | 2.91 | 2.77 |
| MgO | 0.99 | 0.58 | 0.56 |
| $Al_2O_3$ | 14.2 | 15.1 | 14.7 |
| $SiO_2$ | 65.2 | 66.7 | 68.3 |
| $P_2O_5$ | 0.14 | 0.22 | 0.23 |
| $K_2O$ | 5.07 | 5.09 | 5.21 |
| CaO | 0.66 | 0.66 | 0.56 |
| $TiO_2$ | 0.30 | 0.30 | 0.28 |
| MnO | 0.04 | 0.04 | 0.05 |
| $Fe_2O_3$ | 3.23 | 2.74 | 2.84 |
| S | 0.01 | 0.01 | 0.01 |
| Sum (%) | 92.78 | 94.31 | 95.40 |
| | Rare earth elements (ppm) | | |
| La | 48 | 24 | 18 |
| Ce | 99 | 50 | 35 |
| Pr | 14.5 | 7.4 | 4.8 |
| Nd | 48.0 | 24.6 | 16.9 |
| Sm | 7.95 | 5.01 | 3.38 |
| Eu | 1.71 | 0.52 | 0.51 |
| Gd | 5.56 | 4.50 | 3.14 |
| Tb | 0.69 | 0.70 | 0.52 |
| Dy | 3.35 | 3.93 | 2.84 |
| Ho | 0.64 | 0.87 | 0.59 |
| Er | 1.20 | 1.78 | 1.18 |
| Yb | 1.20 | 2.14 | 1.26 |
| Lu | 0.2 | 0.3 | 0.2 |
| | Trace elements (ppm) | | |
| Rb | 206 | 542 | 405 |
| Ba | 605 | 178 | 201 |
| Th | 24.9 | 14.8 | 8.7 |
| Ta | 2.24 | 5.94 | 5.23 |
| Nb | 16 | 23 | 16 |
| Ce | 99 | 50 | 35 |
| Sr | 160 | 36 | 51 |
| Hf | 4.6 | 3.2 | 2.5 |
| Zr | 151 | 96 | 70 |
| Sm | 7.95 | 5.01 | 3.38 |
| Y | 13.4 | 20.8 | 14.9 |
| Yb | 1.20 | 2.14 | 1.26 |

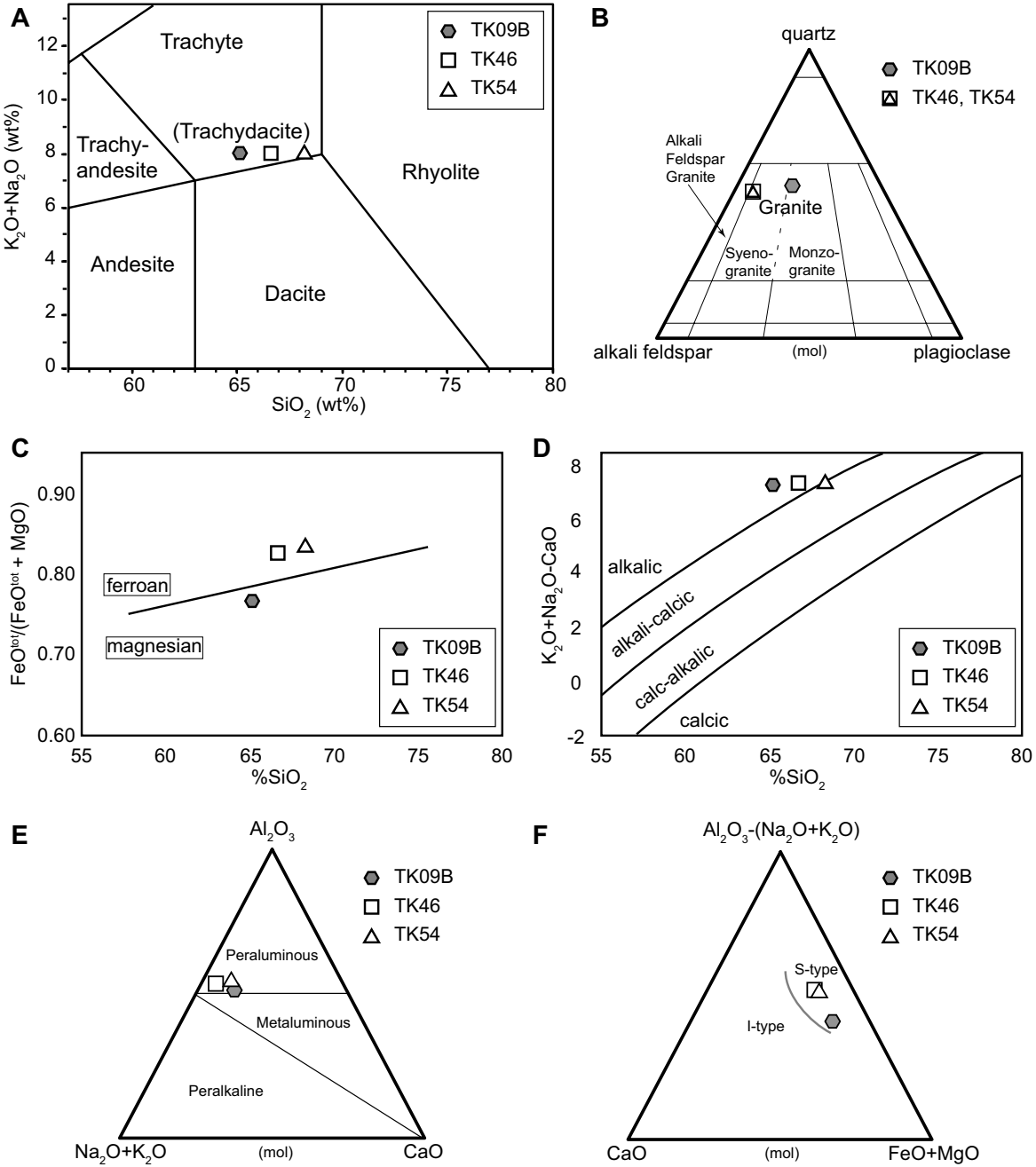


**Figure 3. Major element and mineralogical differentiation plots for the Melung-Salleri (TK46, TK54) and Suri Dobhan (TK09B) orthogneisses. (A) International Union of Geological Sciences classification diagram. (B) QAP (quartz, alkali feldspar, plagioclase feldspar) classification diagram. (C) Fe* diagram of Frost et al. (2001). (D) Modified alkali index plot of Frost et al. (2001). (E) $Al_2O_3$-($Na_2O$ + $K_2O$)-CaO plot for assessment of aluminous nature. (F) $Al_2O_3$-($Na_2O$+ $K_2O$)-CaO-FeO + MgO diagram (Hine et al., 1978).**

The analyzed specimens are also highly potassic, with $K_2O/Na_2O$ ratios of 1.74 (TK09B), 1.75 (TK46), and 1.88 (TK54) (Table 1). Both units show high molar A/CNK ratios of 1.24 for TK09B and 1.31 for TK46 (+TK54), indicating their peraluminous nature (Fig. 3E; Table 1). The Suri Dobhan and Melung-Salleri augen gneiss specimens contain high $SiO_2$ and low CaO (0.56%–0.66%), and significant muscovite (8%–15%), also supporting a crustal derivation. Moreover, when plotted on an $Al_2O_3$-($Na_2O$ + $K_2O$)-CaO-FeO + MgO diagram both units plot in the domain of S-type granite (Fig. 3F).

## Trace and Rare Earth Element Results and Interpretation

Although the major element chemistry of the two bodies is generally similar, the slight differences seen in the major element plots manifest as significant differences in trace element abundance. Primitive mantle-normalized trace elements patterns (Fig. 4A) reveal large negative anomalies in Ba and Sr and a moderate anomaly in Nb in all specimens. A plot of Rb/Sr versus Ba (Fig. 4C) can be used to assess the contribution of major phases to (or from) the melt by the variation in constituent trace elements. TK09B displays very low Rb/Sr and high Ba, whereas TK46 and TK54 show much greater Sr and Ba depletion, resulting in higher Rb/Sr and lower Ba. The ratios for TK09B are suggestive of a vapor-present melt reaction where Sr, contributed to the melt by micas (and/or plagioclase), is not further removed from the melt. Contrary to this, the higher Rb/Sr and relatively low Ba of TK46 and TK54 are more consistent with vapor-absent melting of a biotite- and muscovite-bearing pelitic protolith, where plagioclase remains as a restitic phase (King et al., 2011; Inger, 1993). This interpretation is corroborated by the flatter rare earth element (REE) trend with strong Eu anomaly, characteristic of restitic plagioclase, displayed by the TK46 and TK54 specimens (Fig. 4B). Moreover, the REE trend

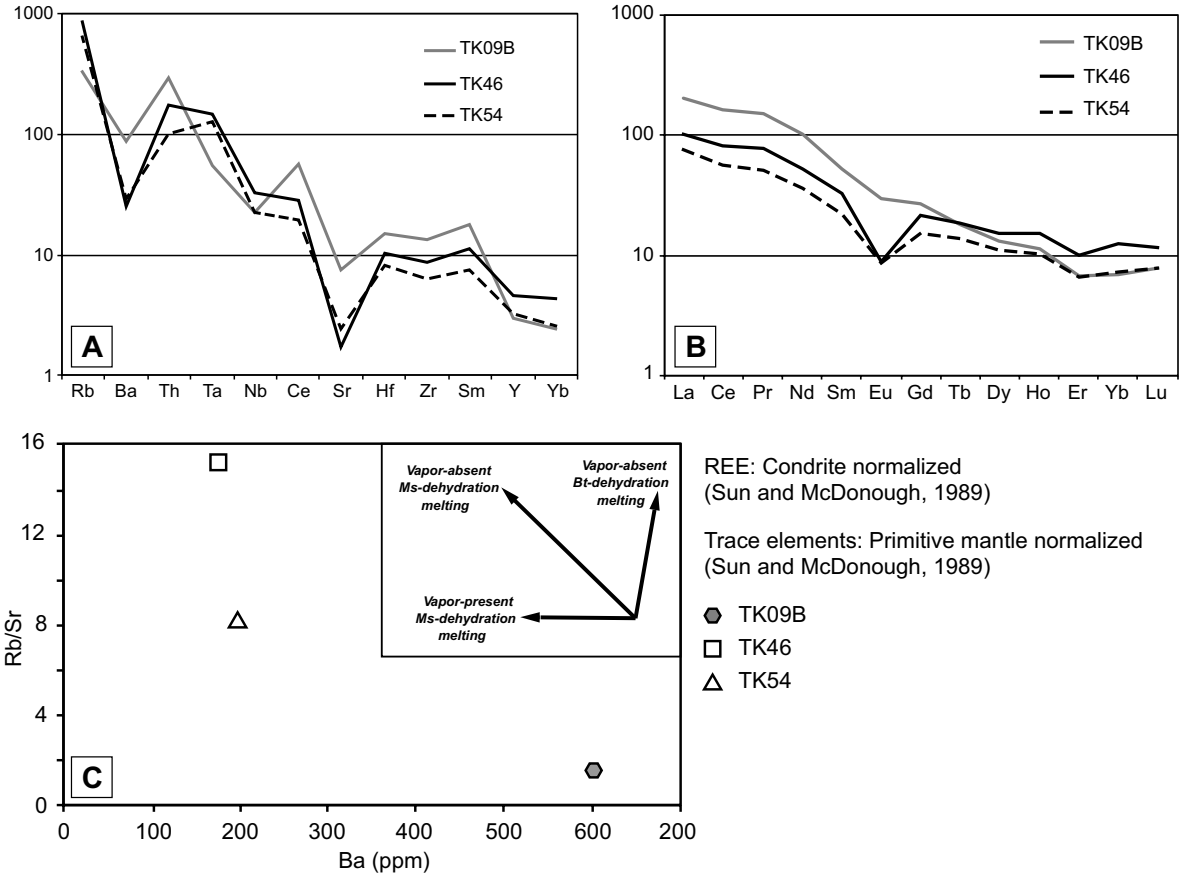


**Figure 4. (A) Trace element plot normalized to Sun and McDonough (1989). (B) Rare earth element (REE) plot normalized to Sun and McDonough (1989). (C) Rb/Sr versus Ba plot. TK46 and TK54 are from the Melung-Salleri orthogneiss, and TK09B is from the Suri Dobhan orthogneiss. Ms—muscovite, Bt—biotite.**

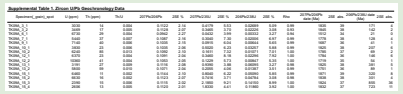

[2]Supplemental Table 1. Zircon U-Pb geochronology data. Please visit http://dx.doi.org/10.1130/GES01293.S2 or the full-text article on www.gsapubs.org to view Supplemental Table 1.

for TK09B is steeper and has no appreciable Eu anomaly (Fig. 4B), consistent with even lower melt fractions and feldspar retention in the restite (±garnet as a restitic phase).

The La, Ce, Pr, Nd, Sm, and Eu concentrations in sample TK09B are higher than in TK46 or TK54, while the amounts of Dy, Ho, Er, Tm, Yb, and Lu in TK09B are between those from the Melung-Salleri specimens (Table 1; Fig. 4B). Large ion lithophile element enrichment reflects derivation from a crustal source as indicated by the major elements. It is interesting that the variations in Fe number and MALI may also be attributed to slight variation in melt conditions, as the magnesian signature in Fe space is most commonly associated with oxidizing conditions, possibly more readily attained in a vapor phase-present reaction, which has also been associated with lower MALI (Frost et al., 2001), both traits displayed by the Suri Dobhan gneiss (TK09B). These observations, plus the association that vapor phase-present melt reactions in melt-prone lithologies generally occur at deeper crustal levels and are favored by increasing pressure (Patiño Douce and Harris, 1998), indicate that TK09B likely formed during prograde conditions.

## U-Th/Pb MONAZITE AND ZIRCON GEOCHRONOLOGY

Four specimens were selected for U-Th/Pb geochronological analysis: Melung-Salleri orthogneiss (TK54), Suri Dobhan orthogneiss (TK09B) and associated leucogranite (TK09A), and Mahabharat Schist (PK199). Specimens from both orthogneiss bodies (TK54 and TK09B), along with a leucogranitic dike crosscutting the Suri Dobhan gneiss (TK09A), were crushed and separated using standard bulk separation methods, whereas the schist specimen (PK199) was prepared as a thin section to preserve textural relationships and grains were analyzed in situ. Both classical laser ablation–multicollector–inductively coupled plasma–mass spectrometry (LA-MC-ICP-MS) and LA split stream (LASS) methods were used to conduct the geochronologic analyses. See the Supplemental File for full details (footnote 1).

In young (Cenozoic) monazite (i.e., grains in PK199), the low abundance of radiogenic $^{207}Pb$ results in relatively imprecise $^{207}Pb/^{235}U$ dates obtained by LA-MC-ICP-MS methods. In addition, $^{206}Pb/^{238}U$ dates typically display reverse discordance as a result of incorporation of excess $^{230}Th$ during crystallization and/or recrystallization (e.g., Schärer, 1984). In this study we report $^{208}Pb/^{232}Th$ ages because Th (and therefore radiogenic $^{208}Pb$) is abundant (>5 wt%) and it does not sustain disequilibrium effects.

### TK54—Melung-Salleri Orthogneiss

Zircons from TK54 are typically clear to slightly cloudy euhedral crystals with faint to moderately well-developed oscillatory zonation in cathodoluminescence (Fig. 5A). We analyzed 34 spots across 27 grains; 5 spots were excluded due to chemical irregularities (high Sr or high Y concentrations) indicating ablation of inclusions. The remaining 29 spots are characterized by low Th/U ratios (average ~0.1) and are all discordant in U-Pb space. Four analyses yield apparent $^{207}Pb/^{206}Pb$ dates older than 2.2 Ga (Supplemental Table 1; footnote 2), whereas the main group of zircons (25 analyses) do not yield a common intercept on a Tera-Wasserburg diagram (Fig. 5B). These same data outline a poorly defined linear array on a standard concordia plot with an upper intercept of 1940 ± 16 Ma (Fig. 5C). We note that the mean square of weighted deviates (MSWD = 12) for the upper intercept is considerably greater than unity, suggesting remaining geologic scatter in the data. We therefore cautiously interpret this age to approximate modal timing of zircon crystallization in this rock. The lower intercept is interpreted to reflect relatively recent time-integrated radiogenic Pb loss.

### TK09B and TK09A—Suri Dobhan Orthogneiss and Leucogranite

Two specimens from the same outcrop of the Suri Dobhan orthogneiss were investigated. TK09B is a sample of the orthogneiss, and TK09A is a partially boudinaged, crosscutting, medium-grained, quartz + feldspar + muscovite + garnet + tourmaline leucogranite dike (see Larson, 2012; Fig. 5A therein). This dike appears to have an associated melanosome and has been interpreted to represent in situ melting of the orthogneiss (Larson, 2012).

Zircons separated from TK09B are typically euhedral with well-developed oscillatory zoning, although distinct cores are present in some specimens (Fig. 5D). We carried out 45 LA-MC-ICP-MS spot analyses across 22 grains; 9 were rejected for inconsistent signal or poor ablation. Two Archean ages are not plotted. The remaining 33 analyses do not define an interpretable intercept on a Tera-Wasserburg diagram (Fig. 5E), but outline a linear array on a Wetherill concordia plot (Fig. 5F). This array is characterized by an upper intercept of 1863 ± 14 Ma (MSWD = 6.5). As discussed for TK54, the MSWD for the upper intercept indicates excess scatter in the data, but likely approximates the timing of zircon crystallization in this rock. The lower intercept is interpreted to reflect recent time-integrated radiogenic Pb loss.

Zircon grains from TK09A are generally euhedral with oscillatory-zoned rims surrounding mottled to cryptically zoned cores (Fig. 5G). We performed 15 LA-MC-ICP-MS analyses on 8 grains. The zircon grains are high in U (average = ~5300 ppm) with low Th/U ratios ranging from 0.0015 to 0.013 (Supplemental Table 1; footnote 2). On a Tera-Wasserburg diagram, analyses plot on a two-component mixing line with an upper intercept of 1858 ± 18 Ma and a lower intercept of 6.3 ± 1.0 Ma (MSWD = 1.5; Fig. 5H). A similar mixing line also is apparent when the zircon data are plotted on a standard concordia diagram with an upper intercept of 1839 ± 10 Ma and a lower intercept of 3.2 ± 3.7 Ma (MSWD = 10.6; Fig. 5I). Because the leucogranite dike is late kinematic with the main Himalayan-related tectonic foliation in the host rock, it is considered to be Cenozoic (Larson, 2012). Therefore, we interpret the upper intercept dates to reflect the crystallization age of zircon in the igneous protolith of the orthogneiss from which the leucogranite was derived. The upper intercepts of both the Tera-Wasserburg and concordia diagrams are within error of that derived directly from the orthogneiss body, TK09B. The lower intercept is interpreted to reflect time-integrated radiogenic Pb loss perhaps related to the emplacement of the dike.

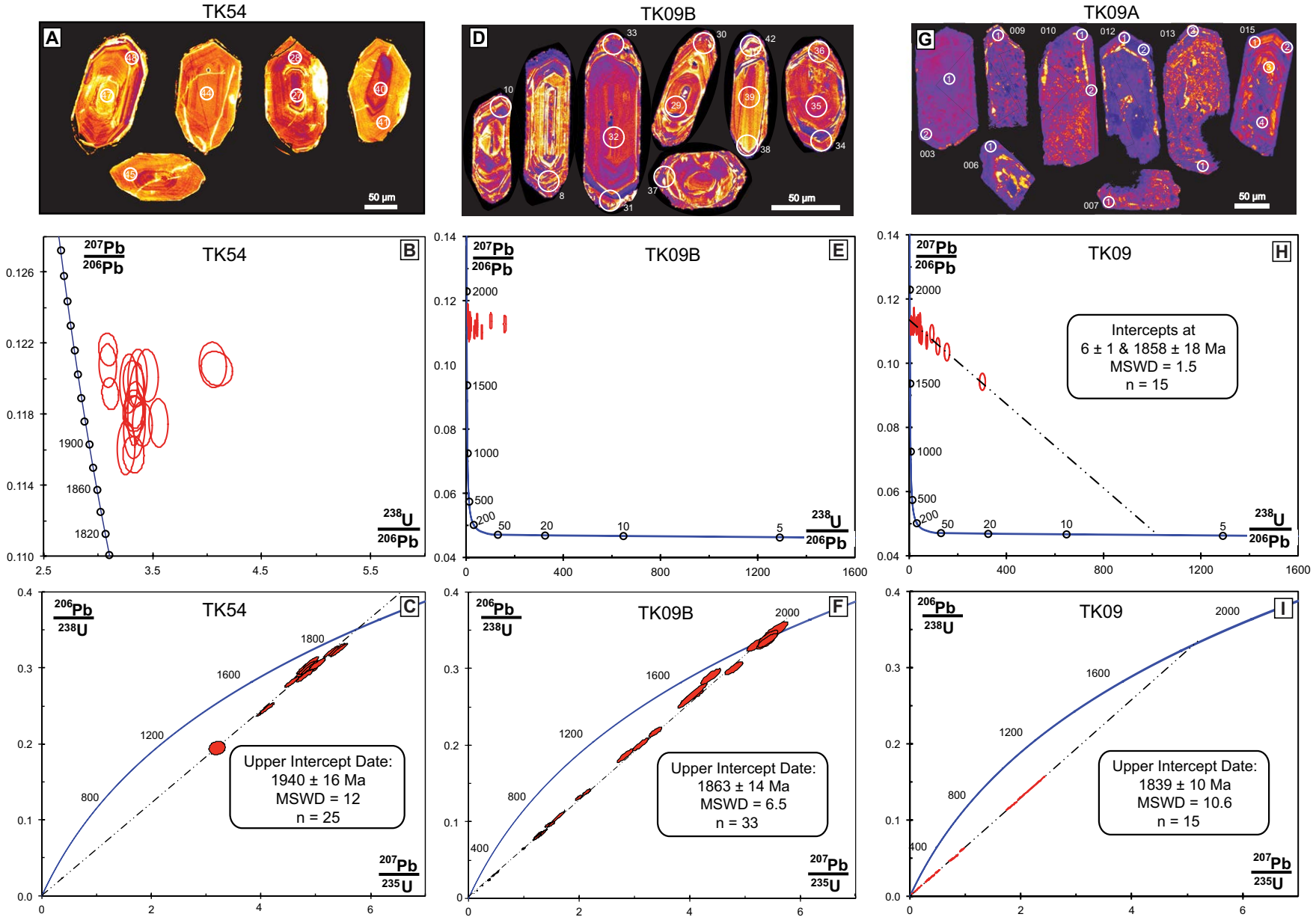


**Figure 5. Laser ablation–inductively coupled plasma–mass spectrometry U-Pb geochronology data for zircon. (A–C) From TK54. (D–F) From TK09B. (G–I) From TK09A. The top row shows example zircon with spot location (numbers correspond to spot number in Supplemental Table 1; see footnote 2) for each specimen. The middle row shows the U-Pb data plotted on Tera-Wasserburg diagrams. The bottom row shows the U-Pb data plotted on Wetherill concordia diagrams. Interpreted dates are indicated. Full data set is available in Supplemental Table 1. MSWD—mean square of weighted deviates.**

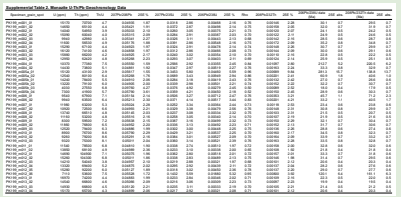

[3]Supplemental Table 2. Monazite U-Th-Pb geochronology data. Please visit http://dx.doi.org/10.1130/GES01293.S3 or the full-text article on www.gsapubs.org to view Supplemental Table 2.

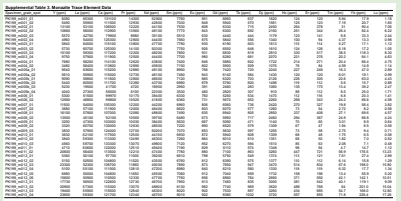

[4]Supplemental Table 3. Monazite trace element data. Please visit http://dx.doi.org/10.1130/GES01293.S4 or the full-text article on www.gsapubs.org to view Supplemental Table 3.

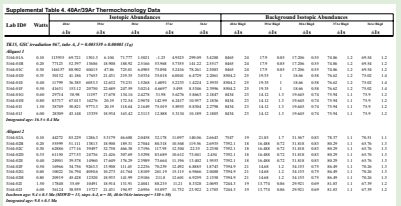

[5]Supplemental Table 4. $^{40}Ar/^{39}Ar$ thermochronology data. Please visit http://dx.doi.org/10.1130/GES01293.S5 or the full-text article on www.gsapubs.org to view Supplemental Table 4.

## PK199—Mahabharat Schist

PK199 is a locally migmatitic garnet and kyanite-bearing, quartz + biotite + K-feldspar + muscovite schist (Figs. 6A–6D) collected from the northern flank of the Mahabharat Range (Figs. 1 and 2). The assemblage is interpreted to comprise prograde garnet + kyanite + K-feldspar perhaps formed through the generalized melting reaction

$$Ms \pm Bt + Pl + Qz \rightarrow Als \pm Grt \pm Kfs + Liq \text{ (Brown, 2010)} \quad (1)$$

or the combination of

$$Ms + Pl + Qz \rightarrow Kfs + Als + Liq \quad (2)$$

and

$$Bt + Pl + Als + Qz \rightarrow Kfs + Grt + Liq \quad (3)$$

(Thompson, 1982; Le Breton and Thompson, 1988),

where Ms is muscovite, Bt is biotite, Pl is plagioclase, Qz is quartz, Als is aluminosilicate, Grt is garnet, Kfs is K-feldspar, and Liq is liquid (mineral abbreviations after Whitney and Evans, 2010).

The dominant foliation, which strikes 075° and dips 25°S, is defined by retrograde biotite and muscovite laths and dynamically recrystallized quartz grains (Figs. 6A, 6B). Biotite and quartz also occur as inclusions within prekinematic garnet grains (Fig. 6C). A grain-shape lineation that plunges 20° toward 175° was also observed. The mica and quartz grains define a compound structural fabric with a through-going C plane that is deflected locally into S planes and cut by C′ extensional shear bands that indicate top-to-the-south shear (Figs. 6B, 6D). Both the metamorphic grade and preserved microstructural fabric in PK199 are similar to those preserved farther north in the main Himalayan range (e.g., Ishida, 1969; Schelling, 1992; Larson, 2012; Larson et al., 2013; From and Larson, 2014; From et al., 2014). To investigate the potential correlation of rocks from the High Himalaya to those in the Mahabharat Range, monazite in specimen PK199 was analyzed to compare its petrochronologic characteristics with published data from High Himalaya HMC rocks. Full geochronoloigc results are reported in Supplemental Table 2 (footnote 3), while trace element results are reported in Supplemental Table 3 (footnote 4).

Monazite displays chemical zoning patterns that typically consist of low-Y cores and high-Y rims (Fig. 7A; Supplemental Fig. 2; footnote 1). The 34 spot analyses using LASS-MC-ICP-MS on 12 matrix grains (Fig. 6A) yielded $^{208}Pb/^{232}Th$ dates that range from 35 to 19 Ma and broadly correlate with chemical zoning patterns (Fig. 7A). Older dates, ca. 35–28 Ma, coincide with low-Y domains, whereas younger dates, ca. 22–19 Ma, coincide with high-Y domains (Fig. 7A). The Gd/Yb ratios also correlate with age, with older dates generally associated with higher ratios and younger dates with lower ratios (Fig. 7B). Intermediate dates, Y concentrations, and Gd/Yb ratios between the two main populations may reflect protracted crystallization and/or recrystallization of monazite under changing geochemical conditions, or apparent dates resulting from mixed sampling of distinct domains (e.g., Larson et al., 2013).

## $^{40}Ar/^{39}Ar$ STEP-HEATING METHODS AND RESULTS

Two specimens from the footwall of the lower discontinuity (TK15 and TK46), one specimen from within the lower discontinuity (TK56), and one specimen from the hanging wall of the lower discontinuity (TK40) were collected for $^{40}Ar/^{39}Ar$ analysis. Specimens were chosen based on the occurrence of macroscopic white mica and structural position to help elucidate what role the structure might have played in the exhumation history of the region. Thin sections from the selected specimens were examined in plane-polarized light (Fig. 8) and imaged using backscattered electrons in a scanning electron microscope. They appear to be chemically homogeneous, with little to no internal deformation and no indication of recrystallization (Supplemental Fig. 4 in the Supplemental File; footnote 1). See the Supplemental File for a complete description of the applied methodologies. Full results are recorded in Supplemental Table 4 (footnote 5) and plotted in Figures 9 and 10. Plateau ages were calculated using MassSpec (Deino, 2001) software using the decay constant of Min et al. (2000), and defined using the following criteria: at least 3 contiguous heating steps that are within 2σ error and that compose ≥50% of $^{39}Ar$ released. Table 2 displays a summary of the results and our interpretations of the $^{40}Ar/^{39}Ar$ ages based on those results. All calculated age results are quoted at 2σ and uncertainties on measurements are 1σ.

The specimen suite yielded interpreted $^{40}Ar/^{39}Ar$ ages ranging from 14.25 to 8.3 Ma (Table 2). Where data yielded statistical plateau ages (TK56, TK40), these are interpreted as the $^{40}Ar/^{39}Ar$ white mica cooling age of the specimens; otherwise, we interpret the integrated ages of relatively homogeneous spectra, or indicated portions thereof, to approximately reflect the same (TK15, TK46). All four specimens displayed some degree of heterogeneity in $^{40}Ar/^{39}Ar$ composition. We discuss this heterogeneity in the following, but in all cases, a dominant $^{40}Ar/^{39}Ar$ apparent age was reflected in multiple aliquots, and coincides with our interpreted ages.

Specimen TK15 is from the base of the Melung-Salleri orthogneiss in the footwall of the lower discontinuity (Figs. 1 and 2); it yielded three heterogeneous age spectra (Fig. 9). Aliquot 1 yielded age steps ranging from ca. 35 to 10 Ma, and the inverse isochron plot (Supplemental Fig. 3; footnote 1) forms two arrays toward nonatmospheric $^{40}Ar$ components. Aliquot 2 yielded a more consistent release spectrum with integrated age 9.8 ± 0.2 Ma, and plotted on an inverse isochron diagram forms a mixing line with an atmospheric $^{40}Ar$ component, yielding an isochron age of 9.4 ± 0.2 Ma (MSWD = 0.9, n = 6, $^{40}Ar/^{36}Ar$ intercept = 302 ± 9), which is our interpreted age for this specimen. Aliquot 3 yielded age steps ranging between ca. 800 and 12.6 Ma, and the inverse isochron diagram indicates a significant nonatmospheric $^{40}Ar$ component (Supplemental Fig. 3; footnote 1). The Ca/K ratios for all three aliquots correlate with age and suggest contamination of the white mica, possibly via fluid or solid inclusions. Thus the older dates obtained in several heating steps of these aliquots reflect extraneous Ar, excess and/or inherited, while we interpret those heating steps forming a mixing line with an atmospheric $^{40}Ar$ component to reflect the Ar cooling age for white mica.

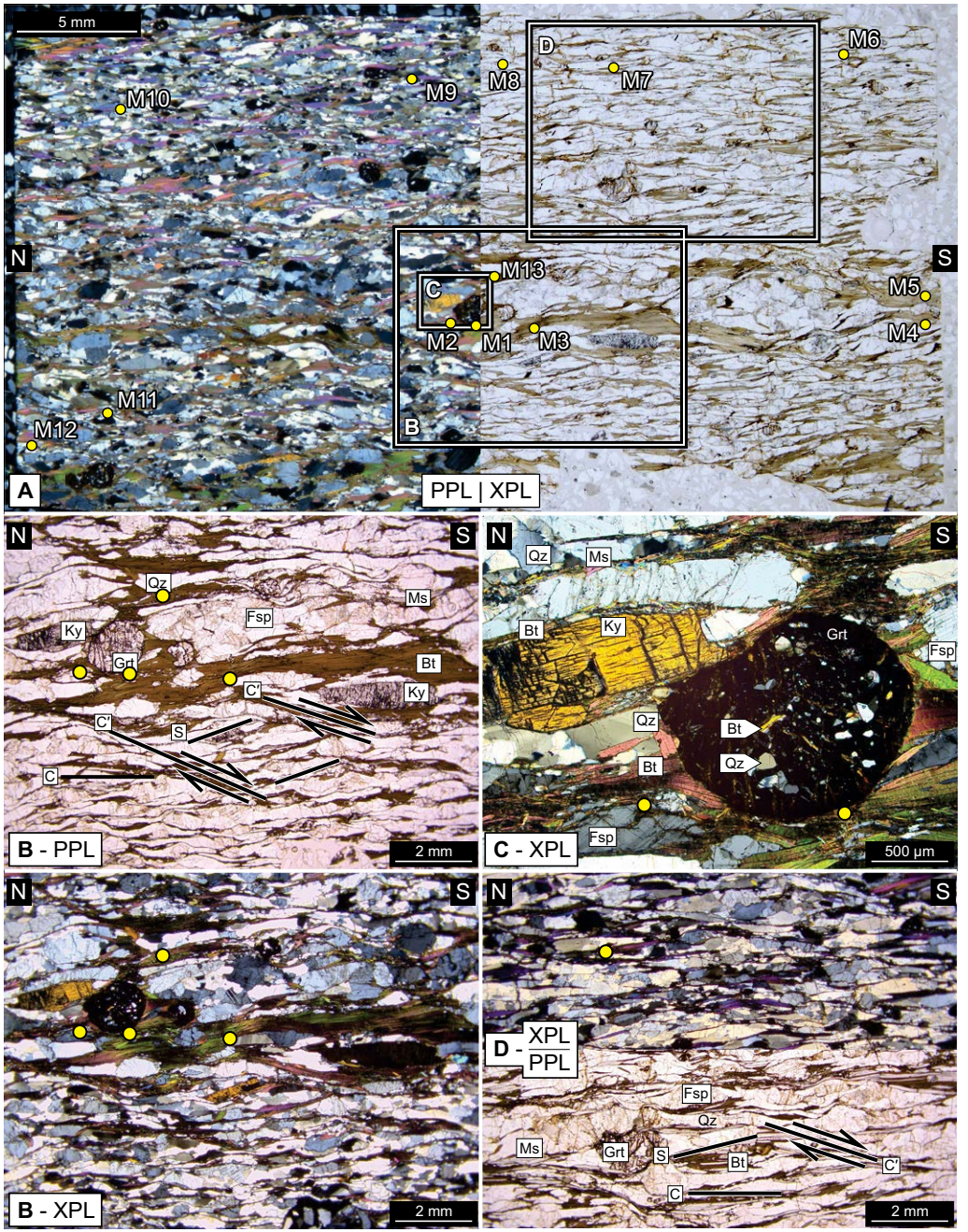


**Figure 6. Photomicrographs of specimen PK199. All photos are oriented with north to the left and south to the right (as marked). (A) Full thin section photomicrograph of PK199 with the locations of more detailed photomicrographs shown. The left half of the thin section is shown in cross-polarized light (XPL) and the right half is shown in plane-polarized light (PPL). Yellow circles indicate the location of monazite (M) grains analyzed. (B) Photomicrograph depicting C/S/C′ fabric indicating top-to-the-south sense shear shown in both PPL (above) and XPL (below) as marked. (C) Photomicrograph in XPL showing the detailed relationships between the major mineral phases. See text for discussion. (D) Photomicrograph, half XPL (top), half PPL (bottom) showing a compound C/S/C′ fabric indicating top-to-the-south shear sense. All mineral abbreviations are after Whitney and Evans (2010).**

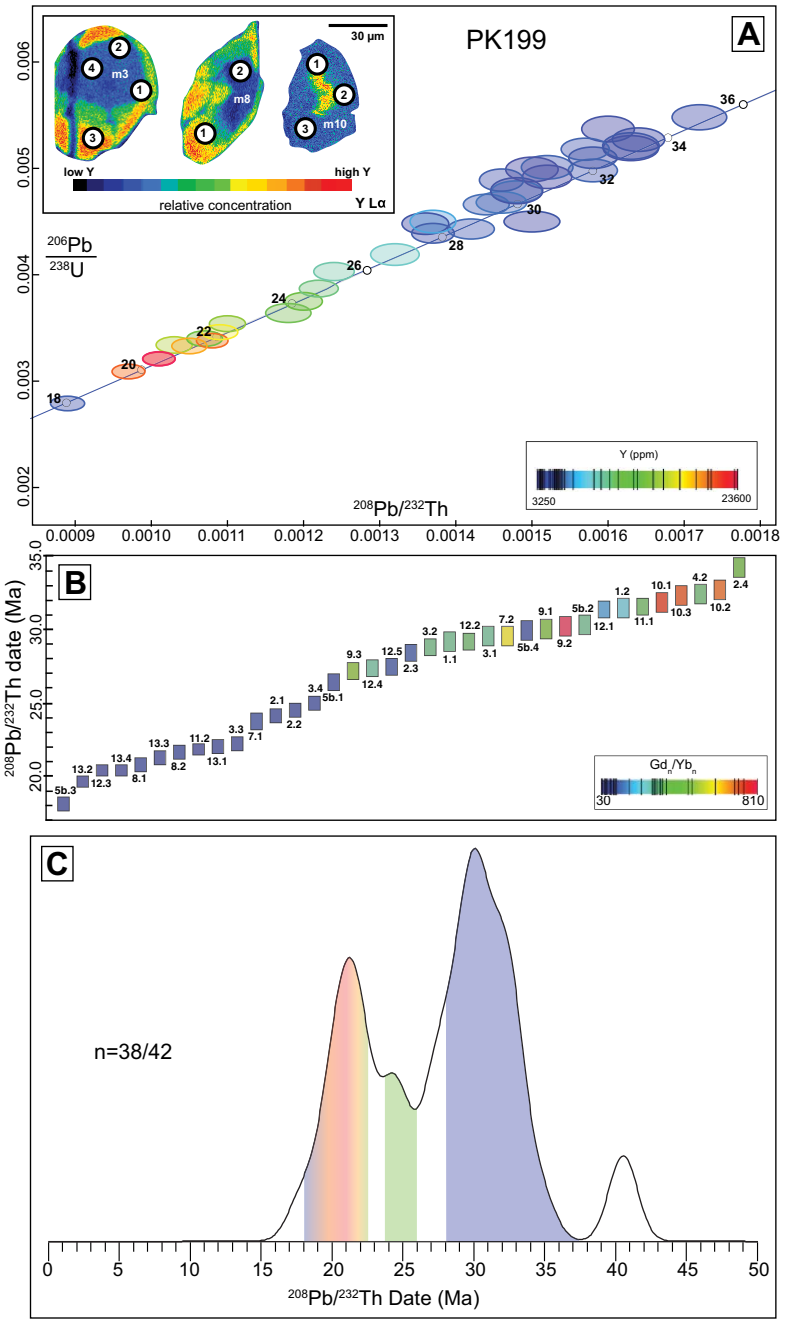


**Figure 7. Laser ablation split stream–inductively coupled plasma–mass spectrometry (LASS-ICP-MS) U-Pb geochronology and rare earth element concentration data for monazite from PK199. Data plots shown in A and B were generated using a modified version of Redux (Bowring et al. [2011]). (A) U-Th-Pb concordia plot colored by Y (ppm). (B) Plot of monazite dates from youngest (left) to oldest (right), colored by $Gd_n/Yb_n$ ratios. (C) Kernal density estimate (KDE) plot generated using DensityPlotter v.7.0 (Vermeesch, 2012). Peaks in the KDE plot are colored for approximate Y (in ppm) as in A. Full data set and complete X-ray maps are available in Supplemental Table 2 (footnote 3) and Supplemental Figure 2 (footnote 1), respectively.**

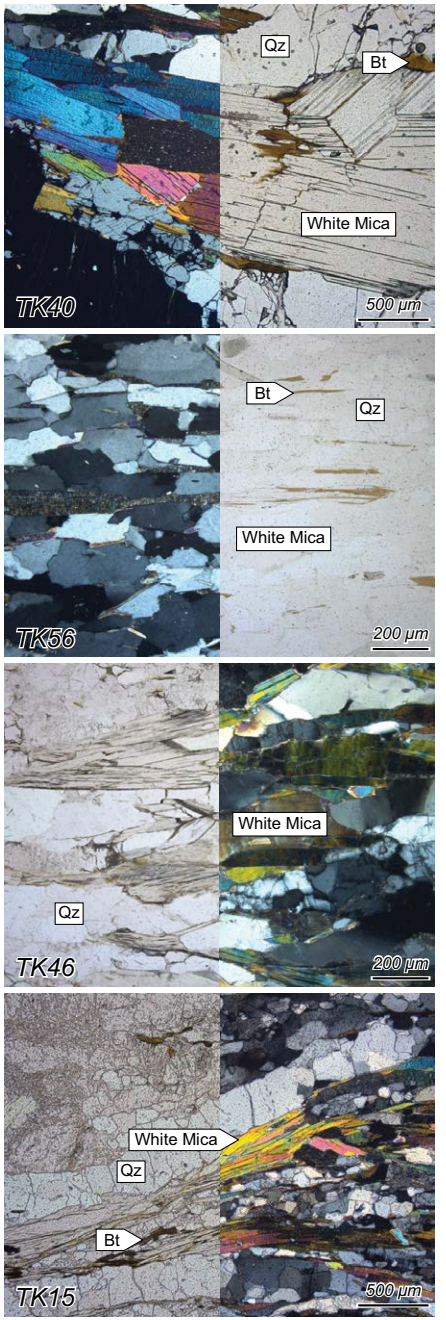


**Figure 8. Photomicrographs of white mica grains in thin section for each specimen. Photomicrographs are presented as half plane-polarized light and half cross-polarized light. Plane-polarized light halves are on the right for TK40 and TK56 and on the left for TK46 and TK15. See text for discussion. Qz—quartz; Bt—biotite.**

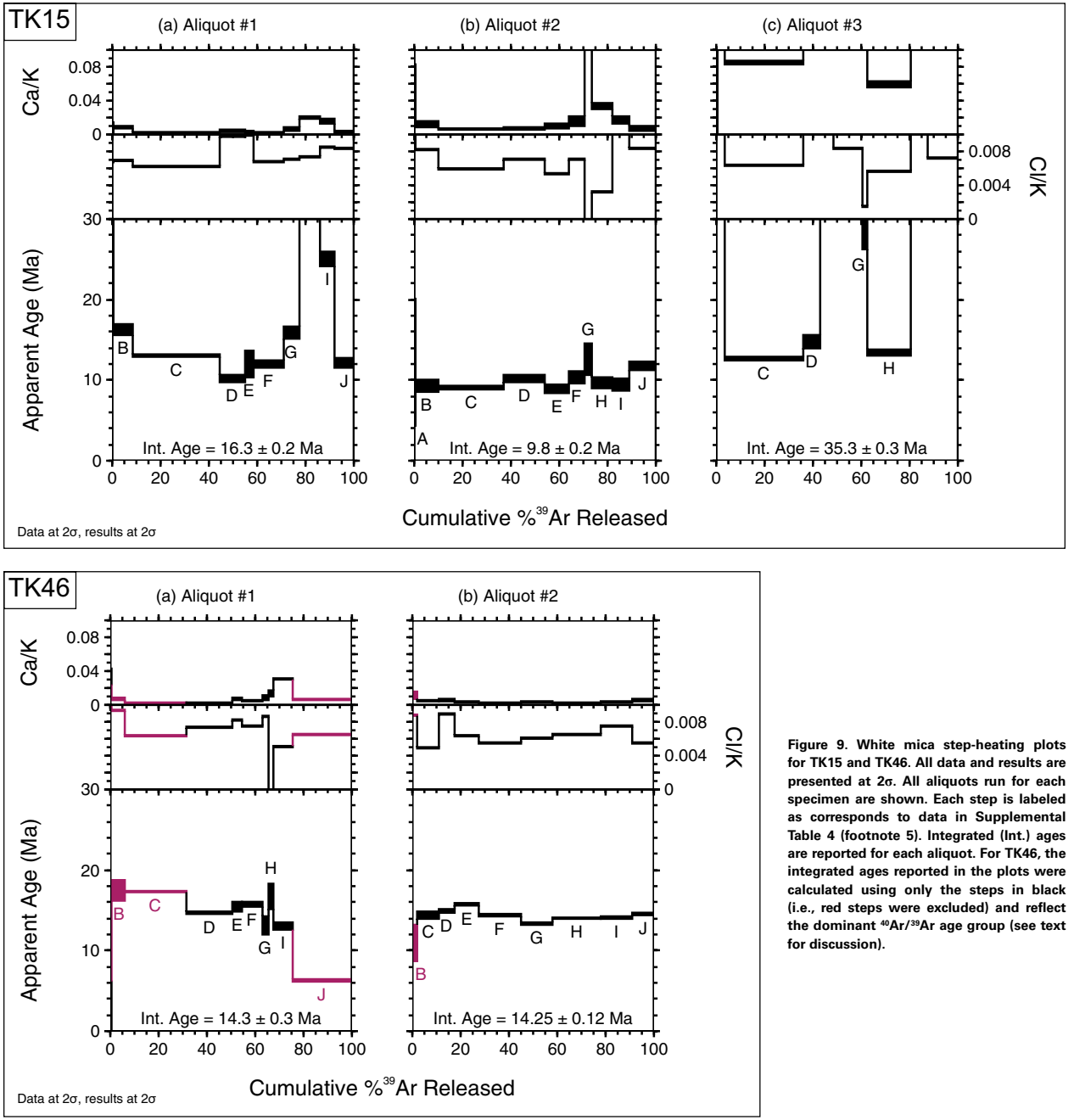


**Figure 9. White mica step-heating plots for TK15 and TK46. All data and results are presented at 2σ. All aliquots run for each specimen are shown. Each step is labeled as corresponds to data in Supplemental Table 4 (footnote 5). Integrated (Int.) ages are reported for each aliquot. For TK46, the integrated ages reported in the plots were calculated using only the steps in black (i.e., red steps were excluded) and reflect the dominant $^{40}Ar/^{39}Ar$ age group (see text for discussion).**

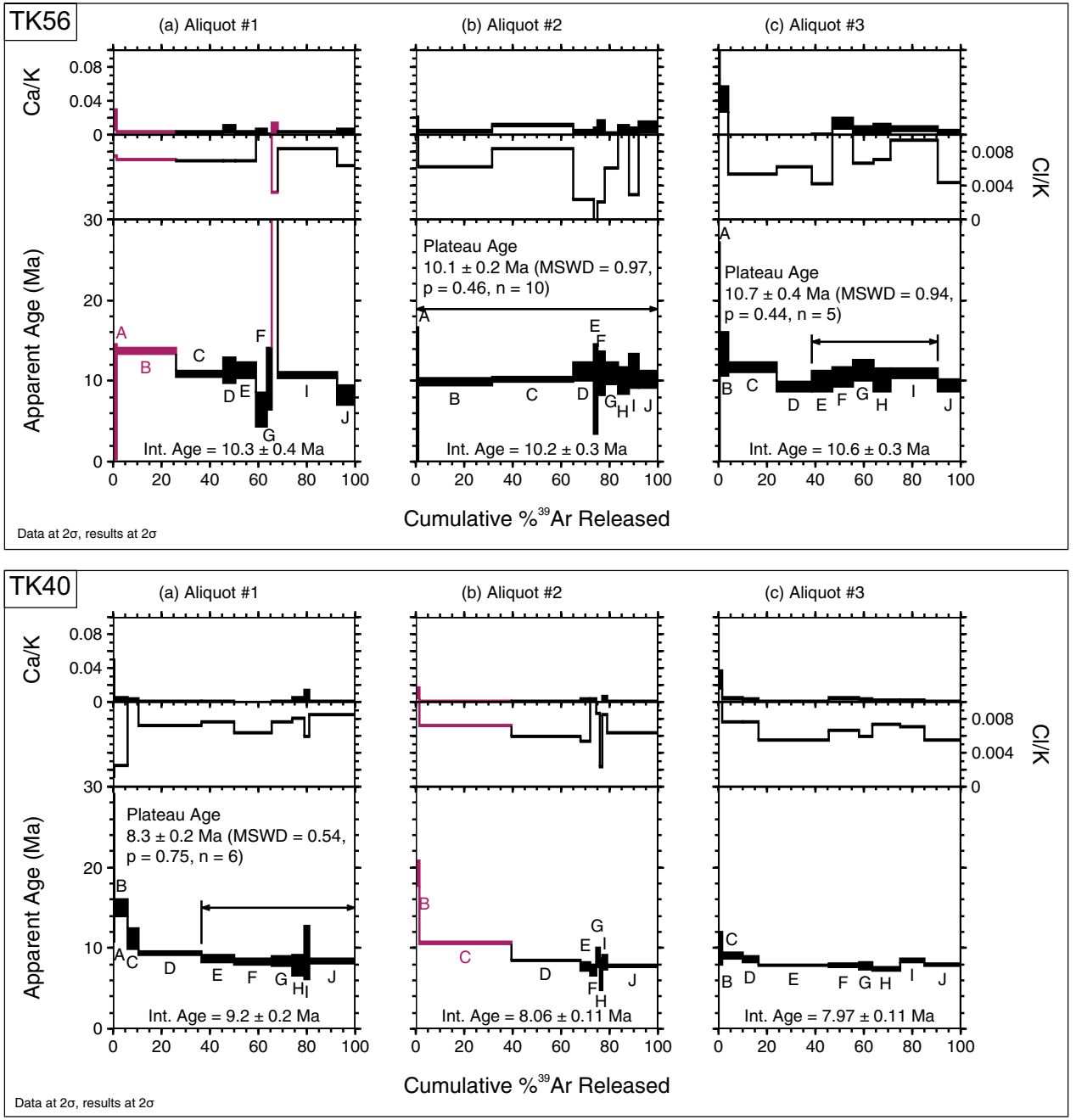


**Figure 10. White mica step-heating plots for TK40 and TK56. All data and results are presented at 2σ. All aliquots run for each specimen are shown. Each step is labeled as corresponds to data in Supplemental Table 4 (footnote 5). The integrated (Int.) ages reported in the plots were calculated using only the steps in black (i.e., red steps were excluded) and reflect the dominant $^{40}Ar/^{39}Ar$ age group (see text for discussion). MSWD—mean square of weighted deviates.**

TABLE 2. SUMMARY OF $^{40}Ar/^{39}Ar$ STEP-HEATING RESULTS AND INTERPRETATIONS

| Sample | GSC Ar# | aliquot | Plateau age (Ma) | 2σ abs. | MSWD | n | Steps | %$^{39}$Ar released | Integrated age* (Ma) | 2σ abs | Isochron age (Ma) | 2σ abs | MSWD | n | $^{40}Ar/^{36}Ar$ intercept | Interpreted age ± 2σ (Ma) |
|---|---|---|---|---|---|---|---|---|---|---|---|---|---|---|---|---|
| TK15 | 3164 | 1 | | | | | | | 16.5 | 0.4 | | | | | | |
| TK15 | 3164 | 2 | | | | | | | 9.8 | 0.3 | 9.4 | 0.2 | 0.9 | 6 | 302 ± 9 | 9.4 ± 0.2 |
| TK15 | 3164 | 3 | | | | | | | 35.3 | 0.3 | | | | | | |
| TK46 | 3165 | 1 | | | | | | | 14.3* | 0.3 | | | | | | |
| TK46 | 3165 | 2 | | | | | | | 14.25* | 0.12 | 14.3 | 0.3 | 16 | 8 | 299 ± 11 | 14.25 ± 0.12 |
| TK56 | 3166 | 1 | | | | | | | 10.3* | 0.4 | 10.9 | 0.3 | 0.5 | 6 | 280 ± 30 | |
| TK56 | 3166 | 2 | 10.1 | 0.2 | 0.97 | 10 | A–J | 100.0 | 10.2 | 0.3 | 10.1 | 0.5 | 1 | 10 | 310 ± 30 | 10.2 ± 0.2 |
| TK56 | 3166 | 3 | 10.7 | 0.4 | 0.94 | 5 | E–I | 52.1 | 10.6 | 0.3 | 10.8 | 0.5 | 1.3 | 7 | 310 ± 30 | |
| TK40 | 3167 | 1 | 8.3 | 0.2 | 0.53 | 6 | E–J | 63.2 | 9.1 | 0.2 | 8.4 | 0.3 | 0.7 | 6 | 300 ± 50 | 8.3 ± 0.2 |
| TK40 | 3167 | 2 | | | | | | | 8.06* | 0.11 | | | | | | |
| TK40 | 3167 | 3 | | | | | | | 7.97 | 0.11 | 7.9 | 0.2 | 4.2 | 8 | 314 ± 12 | |

*Note:* The quoted interpreted ages discussed in the text are listed in the final column and correspond to the plateau age or in the absence of a plateau age, the preferred age (see text for discussion). GSC Ar—Geological Survey of Canada; MSWD—mean square of weighted deviates; abs—absolute.

*Denotes that the integrated age is modified to exclude obvious old and young age outliers; steps used to calculate integrated ages for these aliquots are indicated in Supplemental Table 4 (see footnote 5).

Specimen TK46 is from near the top of the Melung-Salleri orthogneiss (Figs. 1 and 2) in the interpreted footwall of the lower discontinuity; it also yielded heterogeneous spectra (Fig. 9). Aliquot 1 yielded age steps ranging from 17.5 to 6.3 Ma, with the intermediate portion of the release spectrum yielding a modified integrated age of 14.3 ± 0.3 Ma (n = 6, steps D–I). Aliquot 2 yielded a smaller range of ages, from 15.6 to 10.9 Ma, and an integrated age (steps C–J) of 14.25 ± 0.12 Ma. The inverse isochron plot for this aliquot (Supplemental Fig. 3; footnote 1) forms a poorly defined two-component mixing array with atmospheric Ar, yielding an isochron age of 14.3 ± 0.3 Ma (MSWD = 16, n = 8, $^{40}Ar/^{36}Ar$ intercept = 299 ± 11). The integrated and isochron ages of aliquot 2 are statistically identical and provide the interpreted age for this specimen.

Aliquot 1 from TK56, a quartzite in which the foliation is marked by muscovite (Fig. 8) from just structurally above the Melung-Salleri orthogneiss (Figs. 1 and 2), yielded a heterogeneous spectrum with step ages ranging from ca. 34 to 6.3 Ma, although ~60% of $^{39}$Ar released yielded ca. 11–10 Ma ages (Fig. 10). The second aliquot analyzed yielded a plateau age of 10.1 ± 0.2 Ma (MSWD = 1.0, n = 10, steps A–J, 100% $^{39}$Ar released), which provides the interpreted age for this sample. A third aliquot provided a similar result, with a plateau age of 10.7 ± 0.4 Ma (MSWD = 0.9, n = 5, steps E–I, 52.1% $^{39}$Ar released). Inverse isochron plots for all three samples indicate mixing with a dominantly atmospheric $^{40}$Ar component (Supplemental Fig. 3; footnote 1).

Specimen TK40 is a kyanite-grade anatexite-bearing paragneiss collected from the hanging wall of the lower discontinuity (Figs. 1 and 2). Muscovite from the specimen yielded downward-stepping staircase spectra, with aliquot 1 providing a plateau age of 8.3 ± 0.2 Ma (MSWD = 0.5, n = 6, steps E–J, 63% $^{39}$Ar released), which is our preferred age for this sample (Fig. 10). Aliquot 2 yielded a similar integrated age of 8.06 ± 0.11 Ma for steps D–J (60.2% $^{39}$Ar released), while aliquot 3 yielded a relatively flat spectrum with integrated age 7.97 ± 0.11 Ma (all steps). Inverse isochron plots for all three samples indicate mixing with a dominantly atmospheric $^{40}$Ar component (Supplemental Fig. 3; footnote 1).

Several of the spectra exhibit either a younging staircase geometry for the initial heating steps (e.g., TK46–1, TK40–1, TK40–2), or a partial saddle spectrum (e.g., TK15–1, TK56–1), indicating a deviation from the dominant radiogenic Ar component toward older ages in each specimen. The old ages obtained from these initial or intermediate steps approach and exceed 20 Ma, the timing of peak metamorphism, which occurred at peak *T* conditions ranging from ~720 °C (TK40) to 625 °C (TK15) (Larson et al. 2013; Larson and Cottle, 2014), well above the theoretical temperature range for thermal diffusion of Ar in white mica (discussed in the following). We interpret these old ages to reflect an excess $^{40}$Ar component that diffused into white mica from metamorphic fluids before and/or as the rocks cooled below their Ar closure temperature, and/or was trapped in fluid inclusions (e.g., Kelley, 2002). This interpretation is favored over inherited $^{40}$Ar as the high metamorphic temperatures of these samples should have allowed for complete degassing of inherited $^{40}$Ar, and also because this $^{40}$Ar component, locally defining a $^{40}Ar/^{36}Ar$ of ~4000 (TK15 in Supplemental Fig. 3; footnote 1), was commonly released from sites of low Ar retentivity (i.e., lowest *T* heating steps) and never from sites of greatest Ar retentivity (i.e., highest *T* heating steps). The interpreted ages we report reflect the dominant $^{40}Ar/^{39}Ar$ components in each sample, and are interpreted to reflect the thermal diffusion-controlled Ar component of the white mica, yielding the $^{40}Ar/^{39}Ar$ cooling age.

In addition, two aliquots (TK46–01 and TK56–01) yielded one anomalously young age step each, both ca. 6.3 Ma. These data may reflect minor

$^{40}$Ar loss, perhaps due to deformation below the closure temperature, but because the data were not reproducible, it is difficult to definitively interpret their potential significance.

## DISCUSSION

### Suri Dobhan and Melung-Salleri Orthogneisses

Both geochemical and geochronologic data indicate that the Suri Dobhan and Melung-Salleri orthogneisses originated as distinct plutonic bodies. The Melung-Salleri protolith appears to be significantly older than Suri Dobhan protolith, with crystallization ca. 1940 ± 16 Ma versus ca. 1863 ± 14 Ma. Moreover, the units record different melting conditions; the Melung-Salleri specimens indicate vapor-absent processes, in contrast to the vapor-present melting indicated in the Suri Dobhan specimen. These differences indicate that structural duplication is not required to explain their close spatial association.

### Timing of Metamorphism in the Mahabharat Range

The monazite ages extracted from the Mahabharat schist examined in this study (PK199) range from 35 to 19 Ma, broadly separable into an early 35–27 Ma population and a later 22–19 Ma population with a few dates in between (Fig. 7). These groups are spatially associated with low-Y (high Gd/Yb) cores, consistent with the sequestration of Y into garnet during prograde metamorphism (Foster et al., 2004; Gibson et al., 2004; Kohn et al., 2005; Pyle et al., 2001) in the late Eocene–early Oligocene, and high-Y (low Gd/Yb) rims, indicative of garnet breakdown and/or melt crystallization freeing Y during retrograde processes (e.g., Kohn et al., 2005; Larson et al., 2011; Yakymchuk and Brown, 2014) in the early Miocene. This pattern is common in monazite age and REE data patterns reported from HMC rocks across the orogen; low-Y cores typically yield late Eocene to early Miocene ages and high-Y rims yield early to middle Miocene ages (Larson and Cottle, 2015; e.g., Cottle et al., 2009; Lederer et al., 2013; Rubatto et al., 2013; Mottram et al., 2014; From et al., 2014; Ambrose et al., 2015; Larson et al., 2013; Kellett et al., 2010). These preliminary results are therefore consistent with models that correlate the metamorphic rocks exposed in the Mahabharat Range with those of similar or higher metamorphic grade in the HMC in the High Himalaya. This has important implications for the kinematics of the orogen, as explored in the following.

### Variation in $^{40}$Ar/$^{39}$Ar Dates

The $^{40}$Ar/$^{39}$Ar dates obtained from specimens in the study area span 6 m.y. Regional variation in $^{40}$Ar/$^{39}$Ar cooling dates of metamorphic white mica may be the result of differences in grain size, and/or differences in cooling rate or history, the latter implying a tectonic control. To assess the potential contribution of these various controls, a set of diffusion experiments was performed using the diffusion modeling program Diffarg (Wheeler, 1996; Warren et al., 2011) and white mica diffusion parameters from Harrison et al. (2009) to constrain closure temperatures for idealized white mica grains. These experiments explored the range of expected dates that could result from variations in grain size (radii of 0.15, 0.25, 0.375, and 0.75 mm) for a range of geologically plausible linear cooling rates (60, 35, and 20 °C/m.y.; Fig. 11). The grain sizes considered bracket the observed characteristics of the specimens analyzed, while the cooling rates were selected to bracket the known geological history of the region, for which rocks cooled from peak *T* of ~700 °C ca. 20 Ma or ~625 °C ca. 10 Ma (Larson et al., 2013). Considering these scenarios, a cooling rate of 20 °C/m.y. must be outside the range of possible linear cooling histories for these rocks (it requires the rocks to be at 300–400 °C at the present time), but was included as an extreme case. Linear cooling histories may be unrealistic and represent an oversimplification, but they are applied here in the absence of more detailed information on cooling paths of the HMC in this region.

The range of ideal Dodson (1973) closure temperatures spans ~435 °C (0.15-mm-radius grain cooling at 20 °C/m.y.) to ~516 °C (0.75-mm-radius grain cooling at 60 °C/m.y.). Those temperatures are at or below estimates of deformation temperatures along the same transect (Larson and Cottle, 2014), indicating that the dates likely reflect cooling and are not affected by later deformation. The maximum difference in $^{40}$Ar/$^{39}$Ar date attributable to grain size differences is ~3 m.y., and requires an unrealistically slow cooling rate of 20 °C/m.y. (Fig. 11). This compares to an observed difference of ~6 m.y. between TK46 (ca. 14 Ma) and TK40 (ca. 8 Ma). The unexplained variation between the maximum experimental and observed age differences indicates

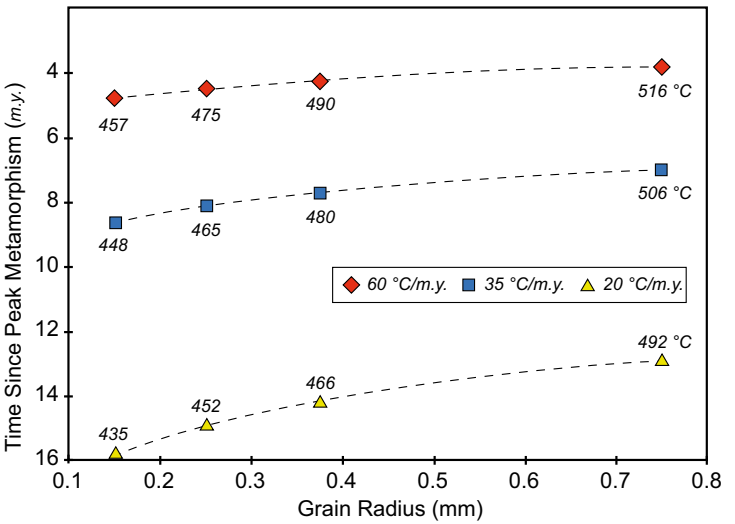


**Figure 11. Plots of model muscovite grain size (horizontal axis) versus time since peak metamorphism (vertical axis). The calculated closure temperature (°C) for each grain size along a linear cooling path is as labeled. See text for discussion.**

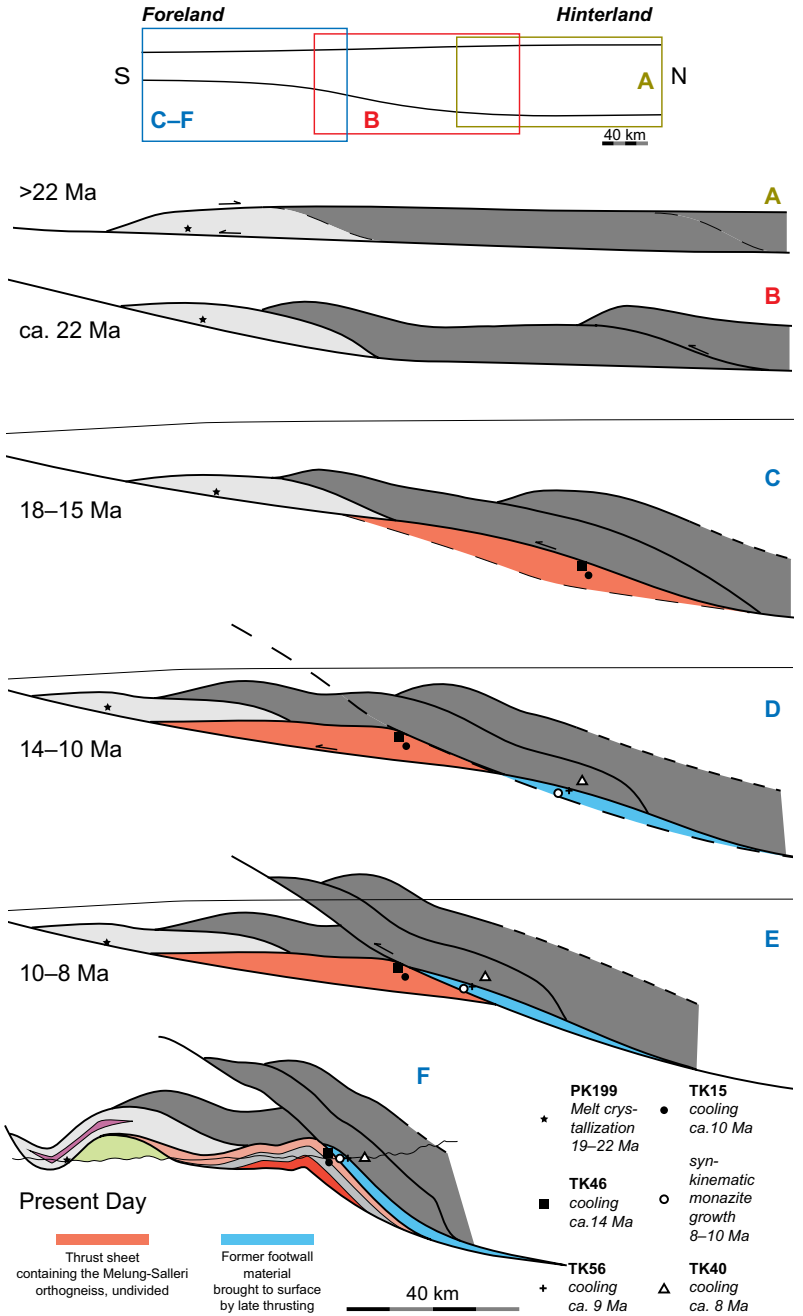


**Figure 12. Schematic kinematic model of the evolution of the map area. See text for discussion. Model is consistent with the data presented herein and previously published constraints. Geologic units are colored as in Figures 1 and 2 except where explained in the figure legend.**

that the rocks did not cool as a single package, and therefore different cooling paths (different in time and/or geometry) are required. Like the monazite petrochronology from the Mahabharat Range, this provides important constraints on the kinematics of the region.

## Kinematic Model

In Figure 12 we present a kinematic model that is consistent with the data presented here as well as constraints previously extracted from the Tama Kosi and nearby regions (From et al., 2014; From and Larson, 2014; Larson, 2012; Larson et al., 2013; Larson and Cottle, 2014). Late Oligocene to early Miocene prograde monazite growth within kyanite- and sillimanite-grade rocks of the High Himalaya in the field area indicates that the exhumed Himalayan middle crust was already at high metamorphic grade at this time (Larson et al., 2013; Larson and Cottle, 2014; From et al., 2014). This overlaps with late Eocene to late Oligocene prograde monazite ages from the Mahabharat Range presented in this study, indicating a coeval metamorphic history. Evidence of similar timing for metamorphism across the orogen at this time outlines a widespread thermal and metamorphic pulse (e.g., Hodges et al., 1996; Hildebrand et al., 1998; Godin et al., 2001; Kohn et al., 2005; Cottle et al., 2009; Kellett et al., 2010; Larson et al., 2011; Lederer et al., 2013; Mottram et al., 2014; Faisal et al., 2014). Moreover, coeval displacement across the structures that bound the top and bottom of the now exhumed mid-crust (the Main Central thrust and South Tibetan detachment system, respectively) indicates lateral extrusion of mid-crustal material at this time (Godin et al., 2006) perhaps as a ductile channel (Beaumont et al., 2004, 2001; Jamieson et al., 2004). South-directed translation of the mid-crust toward the orogenic wedge tip (paired with erosion) facilitated the decompression of the high-grade rocks in the Mahabharat Range in the early Miocene (Figs. 12B, 12C), followed by those of the High Himalaya in the study area in the middle Miocene (Fig. 12C; Larson et al., 2013; From et al., 2014). This continued convergence and southward translation of material over the Indian craton buried rocks in the footwall (Fig. 12C). The $^{40}Ar/^{39}Ar$ white mica cooling age of 14 Ma from the Paleoproterozoic Melung-Salleri orthogneiss indicates pre–14 Ma peak metamorphism (Fig. 12D). The 4 m.y. disparity in $^{40}Ar/^{39}Ar$ white mica ages from the Melung-Salleri orthogneiss specimens TK46 (ca. 14 Ma) and TK15 (ca. 10 Ma) may reflect large variability in thermal structure within the rock unit. Specimen TK46, which now is at the top of the rock unit, also occupies a more forelandward position. This may have allowed it to cool earlier than the structurally lower and more hinterlandward TK15. A possible explanation for the significant difference in cooling ages is that after TK46 cooled sufficiently to retain Ar, foreland translation along the basal thrust stalled, leaving TK15 to cool later through isothermal relaxation and/or erosional exhumation. Alternatively, it could reflect perturbation of isotherms in the immediate footwall of a thrust (see following) maintaining TK15 above its Ar retention temperature for significantly longer than TK46.

Staurolite-grade rocks found structurally above the Melung-Salleri orthogneiss, but below kyanite-bearing rocks of the HMC, were metamorphosed

and deformed at 10–8 Ma (Larson et al., 2013), at least partially coeval with cooling of TK15. In addition, $^{40}Ar/^{39}Ar$ dating of muscovite from the kyanite- and sillimanite-bearing rocks structurally above the staurolite-grade rocks yield late Miocene (9–8 Ma) cooling ages. This juxtaposition of rocks with distinct histories may be explained through the underthrusting and metamorphism of the protolith to the staurolite-grade rocks (Fig. 12D) and their subsequent incorporation into the hanging wall of an out-of-sequence thrust (Fig. 12E). Underthrusting and/or overriding of the staurolite-grade rocks would have juxtaposed them subjacent to higher grade material already well along its retrograde path. The out-of-sequence thrust may have initiated in response to stalling of foreland propagation in the middle Miocene, as perhaps reflected in the variation in cooling ages within the Melung-Salleri orthogneiss. The final structural geometry of the region is interpreted to reflect folding of the exhumed HMC during the migration of deformation toward the foreland and development of the Lesser Himalayan duplex (e.g., McQuarrie et al., 2014; Robinson, 2008).

The position of an out-of-sequence thrust structure that exposes middle to late Miocene metamorphic rocks in its hanging wall and juxtaposes them atop rocks with a different metamorphic history in its footwall is consistent with a reinterpretation of the quartz crystallographic fabric temperature data of Larson and Cottle (2014). These data outline a sharp break in temperature between specimens TK46 (640 ± 50 °C) and TK56 (515 ± 50 °C; Figs. 1, 2, and 13). As previously outlined, this break was originally interpreted to mark a tectonometamorphic discontinuity between kyanite-grade and staurolite-grade rocks with different metamorphic histories (Larson and Cottle, 2014). While such a discontinuity does exist, it was active at temperatures of 610–640 °C (Larson et al., 2013), consistent with deformation temperatures from TK46. The significantly lower deformation temperatures (i.e., TK56) from structurally higher specimens are herein reinterpreted to reflect later, lower temperature deformation and dynamic recrystallization of quartz in the immediate hanging wall of the out-of-sequence thrust as it evolved (Fig. 13).

A similar upward increase in deformation temperatures in the hanging wall of the interpreted late thrust also occurs in the footwall (Fig. 13). At the lowest structural level exposed in the mapped area, which notably contains evidence of anatexis (TK09A), deformation temperatures are estimated as 505 ± 50 °C and increase near linearly toward TK46 at 640 ± 50 °C (Fig. 13; Larson and Cottle, 2014). Given the similarity of this pattern to the pattern that marks the occurrence of a thrust higher in the structural section, it could indicate an additional thrust just below the level of exposure in the field.

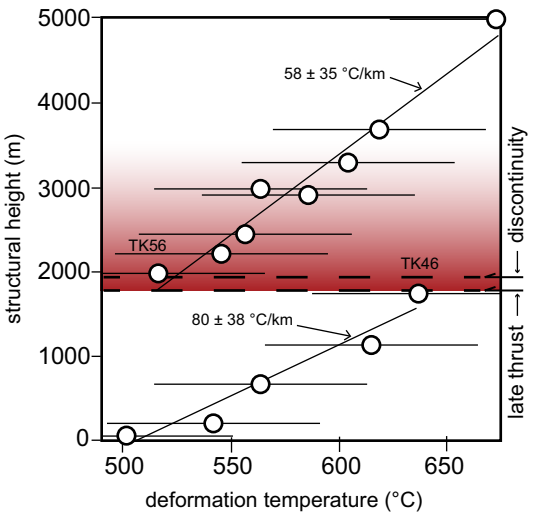


**Figure 13. Published deformation temperatures from the study area shown as a function of structural position (modified from Larson and Cottle, 2014). The approximate locations of the tectonometamorphic discontinuity and late thrust are shown. Thin horizontal black lines show approximate errors (±50 °C) associated with deformation temperature estimates. Gradient represents dynamic recrystallization in the hanging wall of the late thrust; hotter color indicates greater recrystallization. See text for discussion.**

## CONCLUSIONS

The results of this study indicate the following.

1. The similar Suri Dobhan and Melung-Salleri orthogneiss units are two distinct bodies within the same structural panel/sheet and do not reflect structural duplication.

2. HMC rocks of the Mahabharat Range have monazite petrochronologic records indistinguishable from HMC rocks observed in the High Himalaya, indicating that they share a similar history.

3. The $^{40}Ar/^{39}Ar$ data from across a previously identified tectonometamorphic discontinuity in the Tama Kosi region may indicate a late out-of-sequence structure compatible with a distinct, though higher temperature break than reported in previously published quartz deformation temperature data.

This kinematic framework accounts for all available geological data for the Tama Kosi region. The construction of such models can provide the basis for increasingly realistic estimates of ductile shortening across the orogen and large-scale strain rate analysis. It also provides insight into how the deformation style of the mid-crust of an orogen may evolve from convergence accommodation via distributed deformation at mid-crustal levels through to discrete localized deformation in the upper crust.

#### ACKNOWLEDGMENTS

This contribution was supported by a Natural Sciences and Engineering Research Council of Canada Discovery grant to Larson, and is based upon work supported by the National Science Foundation under grant EAR-1119380 to Cottle. Field support was provided by A. Larson, D. Larson, and J. Larson with logistical support from T. Tamang and P. Tamang. We thank N. Joyce and L. Cataldo for help with laboratory analyses at the Geological Survey of Canada (GSC). This is GSC contribution #20160109. Reviews by C. Beaumont, B. Jamieson, and three anonymous referees, and conversations with F. Gervais and C. Guilmette helped improve this manuscript.

#### REFERENCES CITED

Ambrose, T.K., Larson, K.P., Guilmette, C., Cottle, J.M., Buckingham, H., and Rai, S., 2015, Lateral extrusion, underplating, and out-of-sequence thrusting within the Himalayan metamorphic core, Kanchenjunga, Nepal: Lithosphere, v. 7, p. 441–464, doi:10.1130/L437.1.

Beaumont, C., Jamieson, R.A., Nguyen, M.H., and Lee, B., 2001, Himalayan tectonics explained by extrusion of a low-viscosity crustal channel coupled to focused surface denudation: Nature, v. 414, p. 738–742, doi:10.1038/414738a.

Beaumont, C., Jamieson, R.A., Nguyen, M.H., and Medvedev, S., 2004, Crustal channel flows: 1. Numerical models with applications to the tectonics of the Himalayan-Tibetan orogen: Journal of Geophysical Research, v. 109, B06406, doi:10.1029/2003JB002809.

Bowring, J.F., McLean, N.M., and Bowring, S., 2011, Engineering cyber infrastructure for U-Pb geochronology: Tripoli and U-Pb_Redux: Geochemistry, Geophysics, Geosystems, v. 12, Q0AA19, doi:10.1029/2010GC003479.

Brown, M., 2010, Melting of the continental crust during orogenesis: The thermal, rheological, and compositional consequences of melt transport from lower to upper continental crust: Canadian Journal of Earth Sciences, v. 47, p. 655–694, doi:10.1139/E09-057.

Carosi, R., Montomoli, C., Rubatto, D., and Visonà, D., 2010, Late Oligocene high-temperature shear zones in the core of the Higher Himalayan Crystallines (Lower Dolpo, western Nepal): Tectonics, v. 29, TC4029, doi:10.1029/2008TC002400.

Cottle, J.M., Searle, M.P., Horstwood, M.S.A., and Waters, D.J., 2009, Timing of midcrustal metamorphism, melting, and deformation in the Mount Everest region of southern Tibet revealed by U(-Th)-Pb geochronology: Journal of Geology, v. 117, p. 643–664, doi:10.1086/605994.

Cottle, J.M., Larson, K.P., and Kellett, D.A., 2015, How does the mid-crust accommodate deformation in large, hot collisional orogens? A review of recent research in the Himalayan orogen: Journal of Structural Geology, v. 78, p. 119–133, doi:10.1016/j.jsg.2015.06.008.

DeCelles, P.G., Robinson, D.M., Quade, J., Ojha, T.P., Garzione, C.N., Copeland, P., and Upreti, B.N., 2001, Stratigraphy, structure, and tectonic evolution of the Himalayan fold-thrust belt in western Nepal: Tectonics, v. 20, p. 487–509, doi:10.1029/2000TC001226.

Deino, A.L., 2001, Users Manual for Mass Spec v. 5.02. Berkeley Geochronology Center Special Publication 1a, 119 p.

Dodson, M., 1973, Closure temperature in cooling geochronological and petrological systems: Contributions to Mineralogy and Petrology, v. 40, p. 259–274, doi:10.1007/BF00373790.

Faisal, S., Larson, K.P., Cottle, J.M., and Lamming, J.L., 2014, Building the Hindu Kush: Monazite records of terrane accretion, plutonism, and the evolution of the Himalaya-Karakoram-Tibet orogen: Terra Nova, v. 26, p. 395–401, doi:10.1111/ter.12112.

Foster, G., Parrish, R.R., Horstwood, M.S.A., Chenery, S., Pyle, J., and Gibson, H.D., 2004, The generation of prograde P–T–t points and paths; a textural, compositional, and chronological study of metamorphic monazite: Earth and Planetary Science Letters, v. 228, p. 125–142, doi:10.1016/j.epsl.2004.09.024.

From, R., and Larson, K.P., 2014, Tectonostratigraphy, deformation, and metamorphism of the Himalayan mid-crust exposed in the Likhu Khola region, east-central Nepal: Geosphere, v. 10, p. 292–307, doi:10.1130/GES00938.1.

From, R., Larson, K.P., and Cottle, J.M., 2014, Metamorphism and geochronology of the exhumed Himalayan midcrust, Likhu Khola region, east-central Nepal: Recognition of a tectonometamorphic discontinuity: Lithosphere, v. 6, p. 361–376, doi:10.1130/L381.1.

Frost, B.R., Barnes, C.G., Collins, W.J., Arculus, R.J., Ellis, D.J., and Frost, C.D., 2001, A geochemical classification for granitic rocks: Journal of Petrology, v. 42, p. 2033–2048, doi:10.1093/petrology/42.11.2033.

Gansser, A., 1964, Geology of the Himalayas: London, Interscience, 289 p.

Gibson, H.D., Carr, S.D., Brown, R.L., and Hamilton, M.A., 2004, Correlations between chemical and age domains in monazite, and metamorphic reactions involving major pelitic phases: An integration of ID-TIMS and SHRIMP geochronology with Y-Th-U X-ray mapping: Chemical Geology, v. 211, p. 237–260, doi:10.1016/j.chemgeo.2004.06.028.

Godin, L., Parrish, R.R., Brown, R.L., and Hodges, K.V., 2001, Crustal thickening leading to exhumation of the Himalayan metamorphic core of central Nepal: Insight from U-Pb geochronology and $^{40}Ar/^{39}Ar$ thermochronology: Tectonics, v. 20, p. 729–747, doi:10.1029/2000TC001204.

Godin, L., Grujic, D., Law, R.D., and Searle, M.P., 2006, Channel flow, ductile extrusion and exhumation in continental collision zones: An introduction, *in* Searle, M.P., ed., Channel Flow, Ductile Extrusion and Exhumation in Continental Collision Zones: Geological Society of London Special Publication 268, p. 1–23, doi:10.1144/GSL.SP.2006.268.01.01.

Groppo, C., Rolfo, F., and Lombardo, B., 2009, P-T Evolution across the Main Central thrust zone (eastern Nepal): Hidden discontinuities revealed by petrology: Journal of Petrology, v. 50, p. 1149–1180, doi:10.1093/petrology/egp036.

Harrison, T.M., Célérier, J., Aikman, A.B., Hermann, J., and Heizler, M.T., 2009, Diffusion of $^{40}Ar$ in muscovite: Geochimica et Cosmochimica Acta, v. 73, p. 1039–1051, doi:10.1016/j.gca.2008.09.038.

He, D., Webb, A., Larson, K.P., Martin, A.J., and Schmitt, A.K., 2015, Extrusion vs. duplexing models of Himalayan mountain building 3: Duplexing dominates from the Oligocene to present: International Geology Review, v. 57, p. 1–27, doi:10.1080/00206814.2014.986669.

Hildebrand, P.R., Noble, S.R., Searle, M.P., Parrish, R.R., and Shakirullah, 1998, Tectonic significance of 24 Ma crustal melting in the eastern Hindu Kush, Pakistan: Geology, v. 26, p. 871–874, doi:10.1130/0091-7613(1998)026<0871:TSOMCM>2.3.CO;2.

Hine, R., Williams, I.S., Chappell, B.W., and White, A.J.R., 1978, Contrasts between I- and S-type granitoids of the Kosciusko Batholith: Journal of the Geological Society [London], v. 25, p. 219–234, doi:10.1080/00167617808729029.

Hodges, K.V., 2000, Tectonics of the Himalaya and southern Tibet from two perspectives: Geological Society of America Bulletin, v. 112, p. 324–350, doi:10.1130/0016-7606(2000)112<324:TOTHAS>2.0.CO;2.

Hodges, K.V., Parrish, R.R., and Searle, M.P., 1996, Tectonic evolution of the central Annapurna Range, Nepalese Himalayas: Tectonics, v. 15, p. 1264–1291, doi:10.1029/96TC01791.

Inger, S., 1993, Geochemical constraints on leucogranite magmatism in the Langtang Valley, Nepal Himalaya: Journal of Petrology, v. 34, p. 345–368, doi:10.1093/petrology/34.2.345.

Ishida, T., 1969, Petrography and structure of the area between the Dudh Kosi and the Tamba Kosi, east Nepal: Geological Society of Japan Journal, v. 75, p. 115–125, doi:10.5575/geosoc.75.115.

Jamieson, R.A., Beaumont, C., Medvedev, S., and Nguyen, M.H., 2004, Crustal channel flows: 2. Numerical models with implications for metamorphism in the Himalayan-Tibetan orogen: Journal of Geophysical Research, v. 109, B06407, doi:10.1029/2003JB002811.

Jessup, M.J., Law, R.D., Searle, M.P., and Hubbard, M., 2006, Structural evolution and vorticity of flow during extrusion and exhumation of the Greater Himalayan Slab, Mount Everest Massif, Tibet/Nepal: Implications for orogen-scale flow partitioning, *in* Law, R.D., et al., eds., Channel Flow, Ductile Extrusion and Exhumation in Continental Collision Zones: Geological Society of London Special Publication 268, p. 379–413, doi:10.1144/GSL.SP.2006.268.01.18.

Johnson, M., 2005, Structural settings for the contrary metamorphic zonal sequences in the internal and external zones of the Himalaya: Journal of Asian Earth Sciences, v. 25, p. 695–706, doi:10.1016/j.jseaes.2004.04.010.

Johnson, M., Oliver, G., Parrish, R.R., and Johnson, S.P., 2001, Synthrusting metamorphism, cooling, and erosion of the Himalayan Kathmandu Complex, Nepal: Tectonics, v. 20, p. 394–415, doi:10.1029/2001TC900005.

Kellett, D.A., and Grujic, D., 2012, New insight into the South Tibetan detachment system: Not a single progressive deformation: Tectonics, v. 31, TC2007, doi:10.1029/2011TC002957.

Kellett, D.A., Grujic, D., Warren, C., Cottle, J.M., Jamieson, R.A., and Tenzin, T., 2010, Metamorphic history of a syn-convergent orogen-parallel detachment: The South Tibetan detachment system, Bhutan Himalaya: Journal of Metamorphic Geology, v. 28, p. 785–808, doi:10.1111/j.1525-1314.2010.00893.x.

Kelley, S., 2002, Excess argon in K-Ar and Ar-Ar geochronology: Chemical Geology, v. 188, p. 1–22, doi:10.1016/S0009-2541(02)00064-5.

King, J., Harris, N.B., Argles, T.W., Parrish, R.R., and Zhang, H.-F., 2011, Contribution of crustal anatexis to the tectonic evolution of Indian crust beneath southern Tibet: Geological Society of America Bulletin, v. 123, p. 218–239, doi:10.1130/B30085.1.

Kohn, M.J., Wieland, M.S., Parkinson, C.D., and Upreti, B.N., 2005, Five generations of monazite in Langtang gneisses: Implications for chronology of the Himalayan metamorphic core: Journal of Metamorphic Geology, v. 23, p. 399–406, doi:10.1111/j.1525-1314.2005.00584.x.

Larson, K.P., 2012, The geology of the Tama Kosi and Rolwaling valley region, east-central Nepal: Geosphere, v. 8, p. 507–517, doi:10.1130/GES00711.1.

Larson, K.P., and Cottle, J.M., 2014, Midcrustal discontinuities and the assembly of the Himalayan midcrust: Tectonics, p. 718–740, doi:10.1002/2013TC003452.

Larson, K.P., and Cottle, J.M., 2015, Initiation of crustal shortening in the Himalaya: Terra Nova, v. 27, p. 169–174, doi:10.1111/ter.12145.

Larson, K.P., Godin, L., and Price, R.A., 2010, Relationships between displacement and distortion in orogens: Linking the Himalayan foreland and hinterland in central Nepal: Geological Society of America Bulletin, v. 122, p. 1116–1134, doi:10.1130/B30073.1.

Larson, K.P., Cottle, J.M., and Godin, L., 2011, Petrochronologic record of metamorphism and melting in the upper Greater Himalayan sequence, Manaslu-Himal Chuli Himalaya, west-central Nepal: Lithosphere, v. 3, p. 379–392, doi:10.1130/L149.1.

Larson, K.P., Gervais, F., and Kellett, D.A., 2013, A P–T–t–D discontinuity in east-central Nepal: Implications for the evolution of the Himalayan mid-crust: Lithos, v. 179, p. 275–292, doi:10.1016/j.lithos.2013.08.012.

Larson, K.P., Ambrose, T.K., Webb, A.A.G., Cottle, J.M., and Shrestha, S., 2015, Reconciling Himalayan midcrustal discontinuities: The Main Central thrust system: Earth and Planetary Science Letters, v. 429, p. 139–146, doi:10.1016/j.epsl.2015.07.070.

Le Breton, N., and Thompson, A.B., 1988, Fluid-absent (dehydration) melting of biotite in metapelites in the early stages of crustal anatexis: Contributions to Mineralogy and Petrology, v. 99, p. 226–237, doi:10.1007/BF00371463.

Lederer, G.W., Cottle, J.M., Jessup, M.J., Langille, J.M., and Ahmad, T., 2013, Time-scales of partial melting in the Himalayan middle crust: Insight from the Leo Pargil dome, northwest India: Contributions to Mineralogy and Petrology, v. 166, p. 1415–1441, doi:10.1007/s00410-013-0935-9.

McQuarrie, N., Tobgay, T., Long, S.P., Reiners, P.W., and Cosca, M.A., 2014, Variable exhumation rates and variable displacement rates: Documenting recent slowing of Himalayan shortening in western Bhutan: Earth and Planetary Science Letters, v. 386, p. 161–174, doi:10.1016/j.epsl.2013.10.045.

Min, K.W., Mundil, R., Renne, P.R., and Ludwig, K.R., 2000, A test for systematic errors in $^{40}Ar/^{39}Ar$ geochronology through comparison with U/Pb analysis of a 1.1-Ga rhyolite: Geochimica et Cosmochimica Acta, v. 64, p. 73–98, doi:10.1016/S0016-7037(99)00204-5.

Montomoli, C., Iaccarino, S., Carosi, R., Langone, A., and Visonà, D., 2013, Tectonometamorphic discontinuities within the Greater Himalayan Sequence in western Nepal (Central Himalaya): Insights on the exhumation of crystalline rocks: Tectonophysics, v. 608, p. 1349–1370, doi:10.1016/j.tecto.2013.06.006.

Montomoli, C., Carosi, R., and Iaccarino, S., 2015, Tectonometamorphic discontinuities in the Greater Himalayan Sequence: A local or a regional feature?, *in* Mukherjee, S., et al., eds., Tectonics of the Himalaya: Geological Society of London Special Publication 412, p. 25–41, doi:10.1144/SP412.3.

Mottram, C.M., Warren, C., Regis, D., Roberts, N.M.W., Harris, N.B., Argles, T.W., and Parrish, R.R., 2014, Developing an inverted Barrovian sequence; insights from monazite petrochronology: Earth and Planetary Science Letters, v. 403, p. 418–431, doi:10.1016/j.epsl.2014.07.006.

Patiño Douce, A.E., and Harris, N., 1998, Experimental constraints on Himalayan anatexis: Journal of Petrology, v. 39, p. 689–710, doi:10.1093/petroj/39.4.689.

Pyle, J.M., Spear, F.S., Rudnick, R.L., and McDonough, W.F., 2001, Monazite-xenotime-garnet equilibrium in metapelites and a new monazite-garnet thermometer: Journal of Petrology, v. 42, p. 2083–2107, doi:10.1093/petrology/42.11.2083.

Robinson, D.M., 2008, Forward modeling the kinematic sequence of the central Himalayan thrust belt, western Nepal: Geosphere, v. 4, p. 785–801, doi:10.1130/GES00163.1.

Robinson, D.M., DeCelles, P.G., and Copeland, P., 2006, Tectonic evolution of the Himalayan thrust belt in western Nepal: Implications for channel flow models: Geological Society of America Bulletin, v. 118, p. 865–885, doi:10.1130/B25911.1.

Robinson, D.M., DeCelles, P.G., Garzione, C.N., Pearson, O.N., Harrison, T.M., and Catlos, E.J., 2003, Kinematic model for the Main Central thrust in Nepal: Geology, v. 31, p. 359–362, doi:10.1130/0091-7613(2003)031<0359:KMFTMC>2.0.CO;2.

Rubatto, D., Chakraborty, S., and Dasgupta, S., 2013, Timescales of crustal melting in the Higher Himalayan Crystallines (Sikkim, Eastern Himalaya) inferred from trace element-constrained monazite and zircon chronology: Contributions to Mineralogy and Petrology, v. 165, p. 349–372, doi:10.1007/s00410-012-0812-y.

Schärer, U., 1984, The effect of initial $^{230}Th$ disequilibrium on young U-Pb ages: The Makalu case, Himalaya: Earth and Planetary Science Letters, v. 67, p. 191–204, doi:10.1016/0012-821X(84)90114-6.

Schelling, D., 1992, The tectonostratigraphy and structure of the eastern Nepal Himalaya: Tectonics, v. 11, p. 925–943, doi:10.1029/92TC00213.

Sun, S.S., and McDonough, W.F., 1989, Chemical and isotopic systematics of oceanic basalts: Implications for mantle composition and processes, *in* Saunders, A.D., and Norry, M.J., eds., Magmatism in the Ocean Basins: Geological Society of London Special Publication 42, p. 313–345, doi:10.1144/GSL.SP.1989.042.01.19.

Thakur, V.C., Jayangondaperumal, R., and Malik, M.A., 2010, Redefining Medlicott-Wadia's main boundary fault from Jhelum to Yamuna: An active fault strand of the main boundary thrust in northwest Himalaya: Tectonophysics, v. 489, p. 29–42, doi:10.1016/j.tecto.2010.03.014.

Thompson, A.B., 1982, Dehydration melting of pelitic rocks and the generation of $H_2O$-undersaturated granitic liquids: American Journal of Science, v. 282, p. 1567–1595, doi:10.2475/ajs.282.10.1567.

Vermeesch, P., 2012, On the visualisation of detrital age distributions: Chemical Geology, v. 312, p. 190–194, doi:10.1016/j.chemgeo.2012.04.021.

Warren, C., Grujic, D., Cottle, J.M., and Rogers, N.W., 2011, Constraining cooling histories: rutile and titanite chronology and diffusion modelling in NW Bhutan: Journal of Metamorphic Geology, v. 30, p. 113–130, doi:10.1111/j.1525-1314.2011.00958.x.

Warren, C., Singh, A.K., Roberts, N.M.W., Regis, D., Halton, A.M., and Singh, R.B., 2014, Timing and conditions of peak metamorphism and cooling across the Zimithang thrust, Arunachal Pradesh, India: Lithos, v. 200–201, p. 94–110, doi:10.1016/j.lithos.2014.04.005.

Webb, A.A.G., Schmitt, A.K., He, D., and Weigand, E.L., 2011, Structural and geochronological evidence for the leading edge of the Greater Himalayan Crystalline complex in the central Nepal Himalaya: Earth and Planetary Science Letters, v. 304, p. 483–495, doi:10.1016/j.epsl.2011.02.024.

Wheeler, J., 1996, DIFFARG: A program for simulating argon diffusion profiles in minerals: Computers & Geosciences, v. 22, p. 919–929, doi:10.1016/S0098-3004(96)00061-1.

Whitney, D.L., and Evans, B.W., 2010, Abbreviations for names of rock-forming minerals: American Mineralogist, v. 95, p. 185–187, doi:10.2138/am.2010.3371.

Yakymchuk, C., and Brown, M., 2014, Behaviour of zircon and monazite during crustal melting: Journal of the Geological Society [London], v. 171, p. 465–479, doi:10.1144/jgs2013-115.

Yakymchuk, C., and Godin, L., 2012, Coupled role of deformation and metamorphism in the construction of inverted metamorphic sequences: An example from far-northwest Nepal: Journal of Metamorphic Geology, v. 30, p. 513–535, doi:10.1111/j.1525-1314.2012.00979.x.

Yin, A., 2006, Cenozoic tectonic evolution of the Himalayan orogen as constrained by along-strike variation of structural geometry, exhumation history, and foreland sedimentation: Earth-Science Reviews, v. 76, p. 1–131, doi:10.1016/j.earscirev.2005.05.004.

Yin, A., and Harrison, T.M., 2000, Geologic evolution of the Himalayan-Tibetan orogen: Annual Review of Earth and Planetary Sciences, v. 28, p. 211–280, doi:10.1146/annurev.earth.28.1.211.